Modeling, Identification, and Control of an Unmanned Surface Vehicle

Christian R. Sonnenburg and Craig A. Woolsey
Department of Aerospace & Ocean Engineering, Virginia Tech, Blacksburg, Virginia 24061
e-mail: sonycrs@vt.edu, cwoolsey@vt.edu

Received 14 June 2012; accepted 24 January 2013

This paper describes planar motion modeling for an unmanned surface vehicle (USV), including a comparative evaluation of several experimentally identified models over a wide range of speeds and planing conditions. The modeling and identification objective is to determine a model that is sufficiently rich to enable effective model-based control design and trajectory optimization, sufficiently simple to allow parameter identification, and sufficiently general to describe a variety of hullforms and actuator configurations. We focus, however, on a specific platform: a modified rigid hull inflatable boat with automated throttle and steering. Analysis of experimental results for this vessel indicates that Nomoto's first-order steering model provides the best compromise between simplicity and fidelity at higher speeds. At low speeds, it is helpful to include a first-order lag model for sideslip. Accordingly, we adopt a multiple model approach in which the model structure and parameter values are scheduled based on the nominal forward speed. The speed-scheduled planar motion model may be used to generate dynamically feasible trajectories and to develop trajectory tracking control laws. The paper describes the development, analysis, and experimental implementation of two trajectory tracking control algorithms: a cascade of proportional-derivative controllers and a nonlinear controller obtained through backstepping. Experimental results indicate that the backstepping controller is much more effective at tracking trajectories with highly variable speed and course angle. © 2013 Wiley Periodicals, Inc.

1. INTRODUCTION

Unmanned surface vehicles (USVs) provide unique capabilities for military and security applications, including harbor patrol, maritime interdiction, and riverine operations. In terms of payload capacity and persistence, USVs offer greater capability than aerial vehicles or underwater vehicles. Thus, USVs can serve a complementary role within a heterogeneous autonomous vehicle network. Besides serving as a potential launch and recovery platform for these lower-endurance vehicles, a USV can provide a mobile interface between air vehicles that communicate using radiofrequency and submerged assets that communicate acoustically. Overviews of recent USV development activities can be found in Manley (2008) and Bertram (2008). Platforms and applications related to defense and security are described in Thomsen et al. (2007).

One application for USVs is rapid mapping of a riverine environment, where waterways may be narrow and nonuniform in depth and flow (Gadre et al., 2009). Such environments may be poorly known because of traffic and debris, shifting bathymetry, variable water levels, new construction, or other factors. A riverine USV, acting alone or in a team, can characterize such an environment, providing bathymetric maps to a human supervisor, for example. To operate in such an environment, however, the USV must be able to autonomously navigate in a dynamic, uncertain waterway. Moreover, to provide a rapid assessment, the perception and maneuvering algorithms must execute quickly and reliably.

This paper focuses on providing a riverine USV with the ability to robustly and accurately execute maneuvers. We first concentrate on USV dynamic modeling as it relates to agile autonomous maneuvering in the confines of a riverine waterway. The objective is to determine a model that is sufficiently rich to enable effective motion planning and control and sufficiently simple to allow straightforward parameter identification. We consider a set of simple models whose parameters can be quickly and easily identified from standard motion data. Analysis of experimental results indicates that Nomoto's first-order steering model, with speed-scheduled parameter values, provides a good compromise between simplicity and fidelity. At low speeds, where sideslip is most noticeable, Nomoto's model is augmented with an additional first-order lag to account for sideslip. This steering model is used in conjunction with a first-order speed model, also scheduled by nominal speed,

Direct correspondence to: Craig A. Woolsey, e-mail: cwoolsey@vt.edu.

15564967, 2013, 30, Downloaded from https://onlinelibrary.wiley.com. By Universita Di Pavia- on [25/11/2021]. Re-use and distribution is strictly not permitted, except for Open Access articles

15564967, 2013, 30, Downloaded from https://onlinelibrary.wiley.com. By Universita Di Pavia- on [25/11/2021]. Re-use and distribution is strictly not permitted, except for Open Access articles

and a constant-parameter thruster model to generate dynamically feasible trajectories for the USV to follow, though the details of trajectory generation are addressed elsewhere (Stilwell et al., 2011). An effective closed-loop control algorithm is then proposed that enables the riverine USV to track trajectories in the presence of environmental disturbances and modeling uncertainties.

1.1. USV Dynamic Modeling

Fossen (1991) provides a review of surface vessel motion models. In addition to the six degree-of-freedom nonlinear motion model, he describes a variety of "maneuvering" models that describe a vessel's motion in a horizontal plane. These are generally based on a combination of physical principles and empirical observations, and they are often decomposed into speed (surge) and steering (sway and yaw) models. The model of Abkowitz (1964) combines the planar rigid body equations with a third-order Taylor series expansion of the hydrodynamic forces and moments. The model of Norrbin (1970) incorporates empirical models for the hydrodynamic effects; a simplified version is described in Blanke (1981). The simplest and most popular steering model is the first-order turn rate model described in Nomoto et al. (1957). Although the model was developed for displacement vessels, it has been applied to semiplaning and planing vessels as well. A deficiency of Nomoto's model is its inability to accommodate slipping motion, an appreciable effect in some operating regimes. The model described in Yu et al. (2008a) expands Nomoto's first-order steering model by including a first-order equation for sideslip. This "Nomoto-with-sideslip" model is of the same order as the linear steering model obtained by linearizing about steady forward motion, but it has fewer parameters; in transfer function form, the Nomoto-with-sideslip model omits a zero that appears in the linearized steering equations. Rolling motion can also be included in a vessel steering model (Amerongen and Cappelle, 1981; Christensen and Blanke, 1986; Son and Nomoto, 1981). While the vessel considered in the present work does undergo appreciable rolling motion while maneuvering in calm water, the effect of this motion on the steering motion can be effectively incorporated into a simpler, planar motion model.

1.2. Model Identification

Identification involves determining parameter values for a structured model of a given system such that input/state histories of the model best match input/state histories of the physical system. System identification is a mature field and the literature is extensive. Popular textbooks on the topic include Jategaonkar (2006), Ljung (1999), Juang (1994), and Morelli and Klein (2006). In general, model parameters are determined by minimizing the error between true and predicted state histories for given input histories. For linear, time-invariant systems, both frequency- and time-domain approaches are common, and determining aerodynamic or hydrodynamic coefficients for vehicle models is a typical application (Sri-Jayantha and Stengel, 1988; Stalford, 1981; Yoon et al., 2004; Yoon and Rhee, 2003). [In these applications, acceleration data used for model identification are often deduced from noisy velocity data through a smoothing process, such as the algorithm described in Savitzky and Golay (1964).] System identification methods applied to surface vessels include frequency-domain approaches (Selvam et al., 2005) and time-domain approaches, such as maximum likelihood (Åström and Källström, 1976; Källström and Åström, 1981), Kalman filtering (Yoon and Rhee, 2003; Yoon et al., 2004), and artificial neural network (black box) methods (Rajesh and Bhattacharyya, 2008). Recursive least-squares identification has been applied to discrete time (Nguyen, 2008) and continuous time models (Muske et al., 2008). A number of methods are applied in (Ødegård, 2009), including maximum likelihood, extended Kalman filtering, frequency-domain methods, and Ljung's prediction error method.

1.3. Trajectory Tracking

A dynamic model, once formulated and identified, can be used to generate dynamically feasible USV trajectories leading toward some desired destination while avoiding detected hazards. Methods for generating these trajectories are presented elsewhere, however we briefly review the approach used in our application. First, we assume the existence of a map of the environment, though one that may be very poorly known. The map is discretized, and uncertainty is represented stochastically, with grid cells assigned an initial probability of containing some hazard. Using this prior map, a path is generated that guarantees convergence to the destination while minimizing the risk of encountering a hazard (Gadre et al., 2012a; Xu et al., 2009). (Once the USV is underway, the map is updated using sonar and laser line scanner data.) Because this path is generated without regard to the vehicle dynamics, it will generally be infeasible. In an additional optimization step, the USV dynamic model is used within an optimization routine to obtain a dynamically feasible trajectory for the USV to follow (Stilwell et al., 2011).

The feasible trajectory serves as a time-varying reference signal for the USV control system. A feedback control algorithm is required to ensure convergence to this trajectory. The development and experimental comparison of surface vessel trajectory tracking methods is a topic of this investigation. We note that a variety of approaches have been proposed, as in Petterson and Egeland (1996), Pettersen and Egeland (1997), Pettersen and Nijmeijer (2000), Petterson and Nijmeijer (2001), Ashrafiuon et al. (2008). Godhavn (1996) and Toussaint et al. (2000) use integrator backstepping to force exponential convergence of a

15564967, 2013, 30, Downloaded from https://onlinelibrary.wiley.com. By Universita Di Pavia- on [25/11/2021]. Re-use and distribution is strictly not permitted, except for Open Access articles

planar vessel to a trajectory. Godhavn (1996) assumes a nonlinear planar surface vessel with forward force and turning moment inputs. Toussaint et al. (2000) expand upon Godhavn (1996) to incorporate a generalized force acting at the rear of the vessel, a model that better captures the effect of a rudder or a steerable thruster. In Ashrafiuon et al. (2008), a sliding mode approach is used to force asymptotic convergence to a trajectory. Control methods for underactuated surface vessels are also presented in Jiang and Nijmeijer (1997), Jiang et al. (2001), Lefeber et al. (2003), Jiang (2002), Do et al. (2002a), and Do et al. (2002b).

1.4. Outline

This paper discusses the identification of a planar dynamic model for a USV with an outboard motor, including nonlinear thruster dynamics and speed-parametrized linear speed and steering models. Identification is accomplished by minimizing a continuous, time-domain error measure, similar to Yoon and Rhee (2003) and Yoon et al. (2004). Experimental model identification and validation results provide a quantitative comparison of the several models we consider. Based on the resulting steering model, two trajectory tracking control laws are proposed. The first is simply a cascade of proportional-derivative (PD) control loops, which adjust the heading and speed reference commands to track the reference trajectory. The second control algorithm is based on a backstepping approach, similar to the approach described in Jiang and Nijmeijer (1997) and Jiang et al. (2001). Additional experimental results provide a quantitative comparison of the two trajectory tracking algorithms.

Section 2 begins with a short description of the test vehicle, followed by a review of the nonlinear dynamic equations describing the planar motion of a rigid surface vessel. Section 3 presents a detailed explanation of the identification method and results, culminating with a dynamic model for speed and steering, parametrized by the nominal speed. Section 4 describes the two trajectory tracking control laws and provides a comparison based on experimental results. Section 5 presents conclusions and an overview of ongoing work.

2. USV DYNAMIC MODELING

The physics of surface vessel motion provides a structure for model identification. Having developed a nonlinear, physics-based model, one may consider this and/or reduced complexity models as candidate models for motion planning and control design. Conventional analysis of the six degree-of-freedom (DOF) motion of a rigid vessel is decoupled into a three DOF "seakeeping" model for pitch, roll, and heave and a three DOF "maneuvering" model for surge, sway, and yaw. The dynamic models considered in this paper are maneuvering models. The water is assumed to be calm and, for initial modeling and identification purposes, currents are neglected. The effects of currents and flow gradients on marine vessel dynamics have been carefully considered in Woolsey (2011) and Thomasson and Woolsey (2013); it is straightforward to incorporate these effects into the USV dynamic model, if necessary.

Although it is standard practice to separate vessel dynamics into maneuvering and seakeeping models, high-speed watercraft do exhibit coupled dynamics. Interactions with head seas may reduce overall stability, resulting in broaching or parametric rolling. Even in calm water, high-speed craft may experience chine walking, porpoising, or sudden large heel phenomena (Faltinsen, 2005). In extensive field testing, the vessel considered in this paper has not exhibited such effects, although it does display nonlinear turning dynamics when decelerating from high-speeds, due to interaction between the wake and the transom of the vessel. The results in Section 4.4 show that the backstepping control law developed in Section 4.3, using a simple vehicle dynamic model, compensates for this wake interaction. For vessels for which nonlinear effects are more apparent, a more sophisticated model would be required.

Hydrodynamicists characterize surface vessel performance in terms of the Froude number $\mathrm{Fr} = U/\sqrt{Lg}$, where U is the operating speed, L is the length of the submerged portion of the hull, and g is the acceleration due to gravity. As Faltinsen (2005) explains, the weight of a vessel operating with a Froude number less than about 0.4 to 0.5 is almost completely supported by the hydrostatic force of buoyancy, a condition called *displacement* mode. At the other extreme, in *planing* mode, the weight of a vessel operating with a Froude number greater than about 1.0 to 1.2 is almost completely supported by a hydrodynamic force that scales roughly with the square of speed. For intermediate values of the Froude number, both the hydrostatic and hydrodynamic force contribute significantly in balancing the vessel's weight, a condition called *semidisplacement* mode. The USV considered in this paper is designed as a planing vessel, but it routinely operates in each of the three modes. A successful modeling effort will adequately capture the variations in vehicle performance over the full range of achievable Froude numbers.

2.1. Ribcraft USV

Virginia Tech has modified a Ribcraft 4.8 Professional boat for autonomous operation (Gadre et al., 2009; Sonnenburg et al., 2010). The Ribcraft is a 15-foot-long, fiberglass-hulled, rigid hull inflatable boat (RIB) with a 50 horsepower, hydraulically steered Honda outboard motor. The motor can propel the boat to roughly 20 knots.

An Ibeo laser line scanner is the primary visual sensor. The line scanner is mounted to a 2-axis servo-actuated gimbal, which is in turn mounted to the aft antenna arch. An attitude and heading reference system (AHRS) mounted on the laser line scanner provides feedback signals for keeping

15564967, 2013, 30, Downloaded from https://onlinelibrary.wiley.com. By Universita Di Pavia- on [25/11/2021]. Re-use and distribution is strictly not permitted, except for Open Access articles

the device level. A DGPS receiver is mounted to the cockpit seat and a vessel AHRS is mounted underneath the seat, which together provide heading, turn rate, course angle, course angular rate, velocity, and position. Note that in still water, sideslip angle can be deduced from course and heading measurements. The onboard computer processes sensor data and outputs control commands, allowing various levels of control, from simple open-loop steering and throttle commands to closed-loop waypoint following, cross-track control, and more complex nonlinear control.

The mission scenario that drove the development of this USV is autonomous navigation in a riverine environment with little or no *a priori* information about the waterway. A high-level controller sends waypoint or trajectory commands, but the path can be quickly replanned when the vehicle encounters unforseen obstructions. The laser line scanner can detect obstacles within a 250-meter radius and within a 150° field of view. A powerful wireless antenna is mounted to the antenna arch, which allows the onboard computer to communicate with a computer on a chase boat. This chase boat computer can send open-loop commands and waypoints. An emergency stop that sets the throttle to idle and stops control of the steering angle is mounted within easy reach of an onboard attendant. There is also a wireless emergency stop if the boat is running without occupants. The Ribcraft USV is shown in Figure 1.

With a fully instrumented vehicle available for testing, we may use directly measured input and state histories for system identification. We assume that the USV operates in a benign environment, at least while model identification data are collected. We assume there are no disturbances due to currents, wind, or waves. Under these assumptions, it is reasonable to consider a maneuvering model in which there are no disturbances in pitch, roll, or heave. In addition, thrust line effects are ignored; we assume that the force of propulsion induces no pitch or roll moment. (In reality, the propulsor on a turning high-speed vessel will typically induce a roll moment that "banks" the vehicle into the turn. Although we ignore this control-induced rolling motion in modeling, we do seek a maneuvering model that adequately captures turning performance.)

Figure 1. Ribcraft USV operating on the Pearl River.

Beginning from a nonlinear three DOF planar motion model, with a propulsive force and a steering moment as inputs, we make several simplifying assumptions to obtain low-order models suitable for identification from experimental data. Important actuator nonlinearities, such as amplitude and rate saturation, are incorporated when identifying parameter values for these simple models.

2.2. Kinematics

The USV is modeled as a rigid hull with an articulated outboard motor. Define a body-fixed reference frame whose x-axis (denoted by the unit vector $\boldsymbol{b}_x$) points forward along the longitudinal axis of the boat, whose y-axis (denoted by the unit vector $\boldsymbol{b}_y$) points to starboard, and whose z-axis ($\boldsymbol{b}_z = \boldsymbol{b}_x \times \boldsymbol{b}_y$) points downward, completing the orthonormal triad. We assume that the USV is symmetric about its longitudinal plane and that the body reference frame is chosen such that the inertia tensor is diagonal: $\boldsymbol{I} = \mathrm{diag}(I_{xx}, I_{yy}, I_{zz})$.

Suppose that the vector $\boldsymbol{x}$ denotes the position of the body frame origin with respect to some inertially fixed reference frame, denoted by the unit vectors $\boldsymbol{i}_x$, $\boldsymbol{i}_y$, and $\boldsymbol{i}_z$. Let $\boldsymbol{R}$ denote the proper rotation matrix that maps free vectors from the body frame to the inertial frame. Let the body vector $\boldsymbol{v} = (u,\ v,\ w)^T$ represent the translational velocity of the body reference frame with respect to the inertial reference frame. Similarly, let $\boldsymbol{\omega} = (p,\ q,\ r)^T$ represent the body angular rate relative to the inertial reference frame. The rigid body kinematic equations are

$$\dot{\boldsymbol{x}} = \boldsymbol{R}\boldsymbol{v}, \tag{1}$$

$$\dot{\boldsymbol{R}} = \boldsymbol{R}\hat{\boldsymbol{\omega}}, \tag{2}$$

where the caret denotes the 3×3 skew-symmetric matrix satisfying $\hat{\boldsymbol{a}}\boldsymbol{b} = \boldsymbol{a} \times \boldsymbol{b}$ for vectors $\boldsymbol{a}$ and $\boldsymbol{b}$. These equations relate the body's translational and rotational velocity to the rate of change of position and attitude. The matrix $\boldsymbol{R}$ is typically expressed in coordinates, using the conventional Euler angles ϕ, θ, and ψ, for example. In this case, the matrix differential equation (2) is replaced by three equations relating $\dot{\phi}, \dot{\theta}$, and $\dot{\psi}$ to $\boldsymbol{\omega}$; see any standard reference on vessel dynamics, such as Fossen (1995) or Lewandowski (2004).

To simplify matters, we will ignore the roll, pitch, and heave dynamics and consider USV motion in the horizontal plane. Figure 2 illustrates the state and input variables for a planar USV model with a gimbaled thruster (e.g., an outboard engine). Referring to Eqs. (1) and (2), the kinematic model for a USV in planar motion in the absence of currents

15564967, 2013, 30, Downloaded from https://onlinelibrary.wiley.com. By Universita Di Pavia- on [25/11/2021]. Re-use and distribution is strictly not permitted, except for Open Access articles

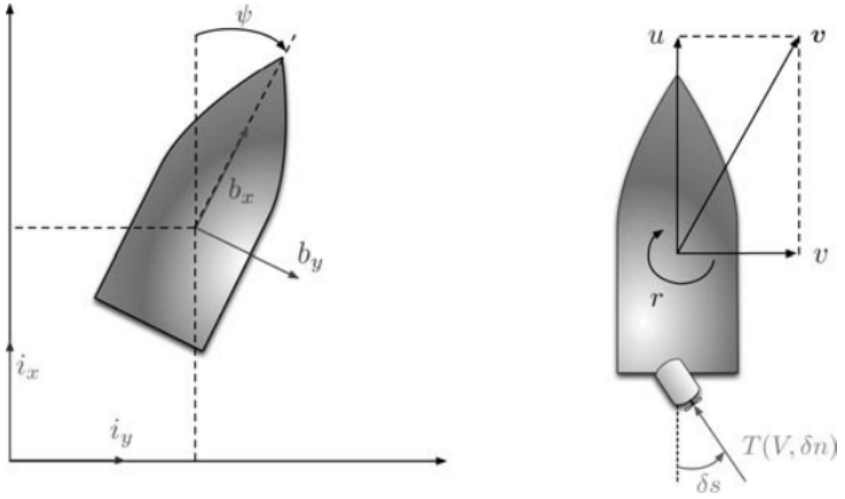

Figure 2. Schematic depiction of a USV.

is

$$\begin{pmatrix} \dot{x} \\ \dot{y} \\ \dot{\psi} \end{pmatrix} = \begin{pmatrix} \cos\psi & -\sin\psi & 0 \\ \sin\psi & \cos\psi & 0 \\ 0 & 0 & 1 \end{pmatrix} \begin{pmatrix} u \\ v \\ r \end{pmatrix}.$$

With the total velocity $V = \sqrt{u^2 + v^2}$, we define the sideslip angle β and the course angle χ as follows:

$$\beta = \arcsin\left(\frac{v}{V}\right) \qquad \text{and} \qquad \chi = \psi + \beta.$$

These definitions are illustrated in Figure 3. Note that the course angle and the heading angle are equal unless the vehicle is slipping. More generally, assuming that there is no ambient flow, the Ribcraft USV's sideslip angle can be deduced using AHRS heading and DGPS course angle measurements. Recognizing that

$$\begin{pmatrix} u \\ v \end{pmatrix} = \begin{pmatrix} \cos\beta & -\sin\beta \\ \sin\beta & \cos\beta \end{pmatrix} \begin{pmatrix} V \\ 0 \end{pmatrix},$$

we may write

$$\begin{pmatrix} \dot{x} \\ \dot{y} \\ \dot{\psi} \end{pmatrix} = \begin{pmatrix} \cos\psi & -\sin\psi & 0 \\ \sin\psi & \cos\psi & 0 \\ 0 & 0 & 1 \end{pmatrix} \begin{pmatrix} \cos\beta & -\sin\beta & 0 \\ \sin\beta & \cos\beta & 0 \\ 0 & 0 & 1 \end{pmatrix} \begin{pmatrix} V \\ 0 \\ r \end{pmatrix}$$

or

$$\begin{pmatrix} \dot{x} \\ \dot{y} \\ \dot{\chi} \end{pmatrix} = \begin{pmatrix} \cos\chi & -\sin\chi & 0 \\ \sin\chi & \cos\chi & 0 \\ 0 & 0 & 1 \end{pmatrix} \begin{pmatrix} V \\ 0 \\ r + \dot{\beta} \end{pmatrix}, \tag{3}$$

where

$$V\cos\beta\,\dot{\beta} = \dot{v} - \dot{V}\sin\beta.$$

The speed-and-sideslip representation provides a useful alternative view, despite the ambiguity in the definition of β when $V \to 0$. Note that Eq. (3) is not really a kinematic model, though, because $\dot{\beta}$ depends on acceleration as well as velocity.

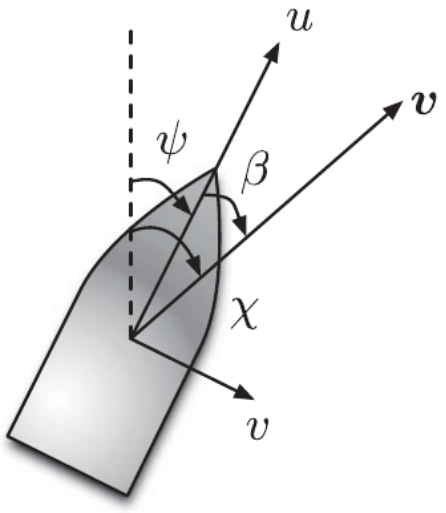

Figure 3. Definitions of sideslip and course angles.

2.3. Dynamics

Adopting Fossen's notation (Fossen, 1991), the planar dynamics of a surface vessel can be described in terms of the configuration and velocity vectors

$$\boldsymbol{\nu} = \begin{pmatrix} u & v & r \end{pmatrix}^T,$$

$$\boldsymbol{\eta} = \begin{pmatrix} x & y & \psi \end{pmatrix}^T,$$

as follows:

$$\boldsymbol{M}\dot{\boldsymbol{\nu}} + \boldsymbol{C}(\boldsymbol{\nu})\boldsymbol{\nu} + \boldsymbol{D}(\boldsymbol{\nu})\boldsymbol{\nu} = \boldsymbol{f},$$

15564967, 2013, 30, Downloaded from https://onlinelibrary.wiley.com. By Universita Di Pavia- on [25/11/2021]. Re-use and distribution is strictly not permitted, except for Open Access articles

where $\boldsymbol{M}$ is a generalized mass matrix, $\boldsymbol{C}$ is the so-called Coriolis and centripetal matrix whose elements are determined from $\boldsymbol{M}$, $\boldsymbol{D}$ is a matrix of damping parameters, and $\boldsymbol{f}$ represents control forces and moments. Note that $\boldsymbol{M}$ and $\boldsymbol{C}$ include contributions from both the rigid body mass and inertia and the added mass and inertia, potential flow theory terms that account for the effort necessary to accelerate the fluid around the vehicle. Details of the nonlinear, physics-based model can be found in Sonnenburg and Woolsey (2010).

For a vessel with a steerable outboard motor, the control forces and moment depend on the propeller speed δn and the steering angle δs. (Details concerning the actuator model are provided shortly.) The three DOF equations of motion are

$$\begin{aligned}(m - X_{\dot{u}})\dot{u} - m(x_G r^2 + vr) + Y_{\dot{v}} vr + \frac{Y_{\dot{r}} + N_{\dot{v}}}{2} r^2 \\ + X_u u + X_{|u|u}|u|u \\ = X_{\text{ctrl}}(\delta s, \delta n),\end{aligned} \tag{4}$$

$$\begin{aligned}(m - Y_{\dot{v}})\dot{v} + (mx_G - Y_{\dot{r}})\dot{r} + (m - X_{\dot{u}})ur + Y_v v + Y_r r \\ + Y_{|v|v}|v|v + Y_{|r|r}|r|r \\ = Y_{\text{ctrl}}(\delta s, \delta n),\end{aligned} \tag{5}$$

$$\begin{aligned}(mx_G - N_{\dot{v}})\dot{v} + (I_{zz} - N_{\dot{r}})\dot{r} + mx_G ur - Y_{\dot{v}} uv - \frac{Y_{\dot{r}} + N_{\dot{v}}}{2} ur \\ + X_{\dot{u}} uv + N_v v + N_r r + N_{|v|v}|v|v + N_{|r|r}|r|r \\ = N_{\text{ctrl}}(\delta s, \delta n).\end{aligned} \tag{6}$$

Throughout the paper, terms of the form $X_{(\cdot)}$, $Y_{(\cdot)}$, and $N_{(\cdot)}$ will represent constant (or "speed-parametrized") coefficients representing the sensitivity of the hydrodynamic surge force, sway force, and yaw moment to changes in the subscript variable, evaluated at some nominal forward speed.

Though the nonlinear equations (4), (5), and (6) are based on physical principles, the hydrodynamic effects are modeled rather simplistically, based on reduced complexity models developed over the years for displacement vessels. The nonlinear model of Abkowitz (1964) includes a third-order truncated Taylor series expansion of the hydrodynamic forces and moment. Reduced complexity variants, in which only the essential, empirically observed hydrodynamic effects are retained, are described in Norrbin (1970) and Blanke (1981). Because of the importance of wave-induced roll coupling in ocean vessel dynamics, a number of models have been developed to capture coupling with this additional degree of freedom (Amerongen and Cappelle, 1981; Christensen and Blanke, 1986; Son and Nomoto, 1981). Considering operations in the relatively confined environment of a river, we neglect any coupling between horizontal plane motions (surge, sway, and yaw) and rolling motion.

We note that the Ribcraft USV described in Section 2.1 routinely operates in each of three modes: displacement, semidisplacement, and planing. As a high-speed vehicle, the USV is subject to a variety of phenomena that are not captured by the simpler models mentioned above, such as porpoising and chine walking (Faltinsen, 2005). These phenomena have not been observed, however, over the (admittedly benign) range of test conditions considered here.

Actuation. The propeller thrust and steering angle define the control forces and moment appearing in Eqs. (4), (5), and (6). A typical outboard motor includes a small vertical vane that provides some additional stability and control, but we assume that propeller thrust generates the entire turning moment.

Thrust T is a function of the vessel speed V and the propeller speed δn (Fossen, 1991):

$$T = cV\delta n + d|\delta n|\delta n, \tag{7}$$

where c and d are constant parameters.

The control forces and moment in Eqs (4), (5), and (6) are

$$X_{\text{ctrl}} = (cV\delta n + d|\delta n|\delta n)\cos\delta s, \tag{8}$$

$$Y_{\text{ctrl}} = (cV\delta n + d|\delta n|\delta n)\sin\delta s, \tag{9}$$

$$N_{\text{ctrl}} = x_{\delta s}(cV\delta n + d|\delta n|\delta n)\sin\delta s, \tag{10}$$

where $x_{\delta s}$ is the longitudinal moment arm from the center of rotation to the pivot point of the thruster.

In the following sections, we present several simplified variants of the dynamic equations (4)–(6) with the actuation model (8)–(10). Again, our objective is to obtain a model that is rich enough to enable effective motion planning and control, simple enough for experimental identification, and general enough to describe a variety of vehicles operating over a large range of speeds.

2.3.1. Speed Dynamics

Linearizing Eq. (4) about the following steady motion:

$$\begin{aligned}u = u_0 \text{ m/s}, \quad v = 0 \text{ m/s}, \quad r = 0 \text{ deg/s}, \\ \delta s = 0 \text{ deg}, \quad \text{and} \quad T = T_0 \text{ N},\end{aligned} \tag{11}$$

one obtains the perturbation dynamics

$$(m - X_{\dot{u}})\Delta\dot{u} = (X_u + 2X_{u|u|}u_0)\Delta u + \Delta T, \tag{12}$$

where

$$\Delta u = u - u_0 \qquad \text{and} \qquad \Delta T = T - T_0.$$

Note that small perturbations in v and r do not affect u; the linearized speed dynamics decouples from the steering dynamics.

Equation (12) provides a first-order linear model relating propeller speed to vehicle speed, in the neighborhood

15564967, 2013, 30, Downloaded from https://onlinelibrary.wiley.com. By Universita Di Pavia- on [25/11/2021]. Re-use and distribution is strictly not permitted, except for Open Access articles

of the nominal condition (11):

$$\Delta\dot{u} = a_u \Delta u + b_u \Delta T. \tag{13}$$

Writing Eq. (13) in terms of the original (nonperturbation) variables gives

$$\dot{u} = a_u u + b_u T - \underbrace{(a_u u_0 + b_u T_0)}_{b_{u_{\text{bias}}}}. \tag{14}$$

Model identification requires finding the three parameters a_u, b_u, and $b_{u_{\text{bias}}}$. This (speed-parametrized) first-order, linear time-invariant system is a standard model for speed dynamics, but others have been proposed; see Breivik et al. (2008) for example.

2.3.2. Steering Dynamics

Having modeled the vessel's motion along the longitudinal axis, it remains to determine a steering model, describing sway and yaw motions. Experimental results suggest a multiple-model approach, where both the model structure and parameter values vary with the vehicle speed. In particular, we find that a low-order model for turn rate and sideslip angle is effective at low speeds, while an even simpler turn rate model suffices at higher speeds. We begin, however, with a more general model obtained by linearizing the physics-based equations.

Linear Steering Dynamics. Linearizing Eqs. (5) and (6) about the steady motion (11) gives

$$\begin{pmatrix} m - Y_{\dot{v}} & 0 & mx_G - Y_{\dot{r}} \\ 0 & 1 & 0 \\ mx_G - N_{\dot{v}} & 0 & I_z - N_{\dot{r}} \end{pmatrix} \begin{pmatrix} \dot{v} \\ \dot{\psi} \\ \dot{r} \end{pmatrix} + \begin{pmatrix} -Y_v & 0 & mu_0 - Y_r \\ 0 & 0 & 1 \\ -N_v & 0 & mx_G u_0 - N_r \end{pmatrix} \begin{pmatrix} v \\ \psi \\ r \end{pmatrix} = \begin{pmatrix} 1 \\ 0 \\ x_{\delta s} \end{pmatrix} T_0 \delta s. \tag{15}$$

Anticipating that there may some bias in the steering dynamics, such that a turning moment is induced even when the the thrust angle is centered, Eq. (15) can be rewritten as follows:

$$\begin{pmatrix} \dot{v} \\ \dot{\psi} \\ \dot{r} \end{pmatrix} = \boldsymbol{A} \begin{pmatrix} v \\ \psi \\ r \end{pmatrix} + \boldsymbol{B} T_0 \delta s + \boldsymbol{B}_{\text{bias}}. \tag{16}$$

There are six unknown elements of the matrices $\boldsymbol{A}$ and $\boldsymbol{B}$, along with two nonzero parameters in $\boldsymbol{B}_{\text{bias}}$, to be determined.

Nomoto's Steering Model. Considering large displacement vessels, Nomoto et al. (1957) suggested that turn rate can be described as a simple first-order equation relating the thrust angle δs to the turn rate r at a given forward speed u_0:

$$\tau \dot{r} + r = K_r \delta s,$$

where

$$K_r = \frac{T_0 x_{\delta s}}{I_{zz} - N_{\dot{r}}}.$$

Adding an integrator to incorporate heading information gives

$$\begin{pmatrix} \dot{\psi} \\ \dot{r} \end{pmatrix} = \begin{pmatrix} 0 & 1 \\ 0 & -\frac{1}{\tau_r} \end{pmatrix} \begin{pmatrix} \psi \\ r \end{pmatrix} + \begin{pmatrix} 0 \\ \frac{x_{\delta s}}{\tau_r (I_{zz} - N_{\dot{r}})} \end{pmatrix} T_0 \delta s + \begin{pmatrix} 0 \\ b_{\text{bias}} \end{pmatrix}. \tag{17}$$

Nomoto's Steering Model with Sideslip. Vessels that steer with a vectored thruster (and possibly a rudder) generally create a nonzero sideslip angle β while turning. Nomoto's model assumes, however, that the vessel is constrained to move in the direction in which it is pointed; it cannot slip while turning. To address this deficiency in the Nomoto model (17) without resorting to the full linearized steering model (16), one can incorporate a first-order lag model for sideslip (Yu et al., 2008b):

$$\tau_\beta \dot{\beta} + \beta = -K_\beta r.$$

Combining with Eq. (17) gives the system

$$\begin{pmatrix} \dot{\beta} \\ \dot{\psi} \\ \dot{r} \end{pmatrix} = \begin{pmatrix} -\frac{1}{\tau_\beta} & 0 & -\frac{K_\beta}{\tau_\beta} \\ 0 & 0 & 1 \\ 0 & 0 & -\frac{1}{\tau_r} \end{pmatrix} \begin{pmatrix} \beta \\ \psi \\ r \end{pmatrix} + \begin{pmatrix} 0 \\ 0 \\ \frac{x_{\delta s}}{\tau_r (I_{zz} - N_{\dot{r}})} \end{pmatrix} T_0 \delta s + \begin{pmatrix} b_{1_{\text{bias}}} \\ 0 \\ b_{2_{\text{bias}}} \end{pmatrix}. \tag{18}$$

The Nomoto with sideslip model has the same dimension as the linear steering model, but with no zero in the turn rate transfer function and no direct throughput from δs to the sideslip dynamics.

At this point, we have introduced a thrust model (7), a linear speed model (13), and three linear steering models: (16), (17), and (18). In Section 3, we discuss methods for experimentally identifying the parameters appearing in these models.

3. MODEL IDENTIFICATION

Model parameter identification for the riverine USV proceeds in two steps. The first step is to determine the steady-state relationship between inputs and outputs from open-loop maneuvers. With these "DC gains" determined, the second step is to identify any additional parameters that govern transient behavior. Inspired by previous system identification efforts for autonomous underwater vehicles (Petrich 2009; Petrich and Stilwell 2011), we implement simple controllers for motion variables of interest (e.g., speed and heading) and obtain closed-loop state histories corresponding to specified, desired output histories (e.g., a square wave in heading angle). Using closed-loop system responses instead of open-loop responses allows more

15564967, 2013, 30, Downloaded from https://onlinelibrary.wiley.com. By Universita Di Pavia- on [25/11/2021]. Re-use and distribution is strictly not permitted, except for Open Access articles

control over the vehicle's motion in the confined operating environments where field tests are performed.

Our approach to model identification, as in Yoon and Rhee (2003) and Yoon et al. (2004), involves adapting model parameter values such that the estimated derivative of the state best matches the experimental data obtained for the feedback controlled USV. Values for the dynamic parameters are obtained using a least-squares cost function. Marine vessel actuators often have nonlinear characteristics such as rate limiting, saturation, time delay, and deadband. For a well-instrumented system, such as the Ribcraft USV, these nonlinear effects can be determined experimentally by comparing actual and commanded inputs.

When estimating model parameters, the question of identifiability naturally arises. For linear dynamic models, as discussed in Petrich (2009), it is sufficient to verify that the system's Markov parameters depend appropriately on the parameters to be identified (Grewal and Glover, 1976). For nonlinear dynamic models, one may consider local identifiability by linearizing around a nominal state. Identifiability analysis is straightforward but is omitted for brevity.

3.1. Identifying Steady-State Input/Output Relationships

To determine the steady-state relationship between inputs and states for a stable system, one applies a constant input and measures the steady-state output. For the vectored thrust USV considered here, the two constant inputs are the thrust angle δs and the propeller speed δn. Performing these steady-state experiments over a range of thrust angles and propeller speeds defines a two-parameter family of steady-state operating conditions.

We begin by considering linear, time-invariant systems with bias, that is, systems of the form

$$\dot{\boldsymbol{x}} = \boldsymbol{A}\boldsymbol{x} + \boldsymbol{B}\boldsymbol{u} + \boldsymbol{B}_{\text{bias}}, \tag{19}$$

where $\boldsymbol{x}(t) \in \mathbb{R}^n$, $\boldsymbol{u}(t) \in \mathbb{R}^m$, and, in a slight abuse of notation, $\boldsymbol{A}$, $\boldsymbol{B}$, and $\boldsymbol{B}_{\text{bias}}$ are real matrices with commensurate dimensions. The identification task is to determine the $n(n+m+1)$ parameters appearing in $\boldsymbol{A}$, $\boldsymbol{B}$ and $\boldsymbol{B}_{\text{bias}}$. A primary requirement is that the resulting parameter values should recover observed steady-state behavior.

Assuming that the matrix $\boldsymbol{A}$ in Eq. (19) is Hurwitz, a constant input $\boldsymbol{u}_{\text{ss}}$ will eventually result in a steady state,

$$\boldsymbol{x}_{\text{ss}} = \boldsymbol{\Phi}\boldsymbol{u}_{\text{ss}} + \boldsymbol{\Phi}_{\text{bias}}.$$

Note that the state matrices $\boldsymbol{A}$ in Eqs. (16), (17), and (18) contain an integrator cascade that gives the heading angle ψ, an ignorable coordinate in the underlying dynamic equations. Omitting the equation for ψ, one obtains Hurwitz state matrices that conform to the system steady-state requirements. For a sufficiently rich set of inputs $\boldsymbol{u}_{\text{ss}}$, one may determine the $n(m+1)$ parameters defining the matrix $\boldsymbol{\Phi} = \boldsymbol{A}^{-1}\boldsymbol{B}$ and the vector $\boldsymbol{\Phi}_{\text{bias}} = \boldsymbol{A}^{-1}\boldsymbol{B}_{\text{bias}}$ from experimental data. These steady-state parameters may be used to constrain the remaining identification process. Noting that

$$\begin{aligned}\boldsymbol{0} &= \boldsymbol{A}\boldsymbol{x}_{\text{ss}} + \boldsymbol{B}\boldsymbol{u}_{\text{ss}} + \boldsymbol{B}_{\text{bias}} \\ &= (\boldsymbol{A}\boldsymbol{\Phi} + \boldsymbol{B})\,\boldsymbol{u}_{\text{ss}} + (\boldsymbol{A}\boldsymbol{\Phi}_{\text{bias}} + \boldsymbol{B}_{\text{bias}})\end{aligned}$$

for m linearly independent inputs, the following $n(m+1)$ linear equations constrain the choice of the $n(n+m+1)$ parameters appearing in $\boldsymbol{A}$, $\boldsymbol{B}$ and $\boldsymbol{B}_{\text{bias}}$:

$$\boldsymbol{0} = \boldsymbol{A}\boldsymbol{\Phi} + \boldsymbol{B}, \tag{20}$$

$$\boldsymbol{0} = \boldsymbol{A}\boldsymbol{\Phi}_{\text{bias}} + \boldsymbol{B}_{\text{bias}}. \tag{21}$$

Incorporating these constraints leaves n^2 free parameters to be determined from dynamic (transient) system response data.

3.2. Identifying Dynamic Parameters

Having found the steady-state parameters appearing in $\boldsymbol{\Phi}$ and $\boldsymbol{\Phi}_{\text{bias}}$, one seeks the remaining "dynamic parameters" appearing in the model (19). We begin with the thruster dynamic model and then describe identification of the steering and speed dynamics.

Because experimental measurements are noisy and state derivatives are not directly measured, an important tool for experimental data analysis is a filter to smooth the data and generate estimates of time derivatives. To simultaneously smooth and differentiate measurements, we use the Savitsky-Golay filter (Savitzky and Golay 1964). This filter uses least-squares regression to fit a polynomial to signal data within a moving window; the time derivative is estimated using the derivative of the polynomial.

3.2.1. Thruster Parameters

In this section, we consider identification of the thruster model (7). Consider the speed dynamics (4) for the case of straight line motion:

$$\dot{u} = \frac{X_u}{(m - X_{\dot{u}})}u + \frac{X_{|u|u}}{(m - X_{\dot{u}})}|u|u + \frac{T}{(m - X_{\dot{u}})}. \tag{22}$$

The parameters $X_{\dot{u}}$, X_u, and $X_{|u|u}$ may be considered coefficients in a polynomial expansion of the hydrodynamic surge force around a nominal condition. Because the USV is a planing vessel, the waterline will vary with the nominal state. These "hydrodynamic derivatives" are therefore parametrized by the nominal forward speed u_0. The thrust term $\tilde{T}$ is

$$\begin{aligned}\tilde{T} &= \frac{T}{m - X_{\dot{u}}} \\ &= \underbrace{\frac{c}{(m - X_{\dot{u}})}}_{\tilde{c}}\,u\delta n + \underbrace{\frac{d}{(m - X_{\dot{u}})}}_{\tilde{d}}\,|\delta n|\delta n.\end{aligned} \tag{23}$$

15564967, 2013, 30, Downloaded from https://onlinelibrary.wiley.com. By Universita Di Pavia- on [25/11/2021]. Re-use and distribution is strictly not permitted, except for Open Access articles

To identify the parameters $\tilde{c}$ and $\tilde{d}$ in Eq. (23), one may isolate dynamics due to thrust by examining the initial response to step inputs in throttle, starting from straight line motion with a steady speed u_0 corresponding to a fixed thrust $\tilde{T}_0$:

$$0 = \frac{X_u}{(m - X_{\dot{u}})} u_0 + \frac{X_{|u|u}}{(m - X_{\dot{u}})} |u_0| u_0 + \tilde{T}_0 . \tag{24}$$

Substituting perturbation values

$$\Delta u = u - u_0 \quad \text{and} \quad \Delta \tilde{T} = \tilde{T} - \tilde{T}_0$$

into the dynamic equation (22) gives

$$\Delta \dot{u} = \frac{X_u}{(m - X_{\dot{u}})}(u_0 + \Delta u) + \frac{X_{|u|u}}{(m - X_{\dot{u}})} \left|(u_0 + \Delta u)\right| (u_0 + \Delta u) + (\tilde{T}_0 + \Delta \tilde{T}).$$

Subtracting the steady-state condition (24), assuming that $u_0 > 0$ is much larger than $|\Delta u|$, and ignoring higher-order perturbation terms leaves

$$\Delta \dot{u} = \tilde{a} \Delta u + \Delta \tilde{T} \quad \text{with} \quad \tilde{a} = \frac{1}{(m - X_{\dot{u}})} (X_u + 2 X_{|u|u} u_0) .$$

It is straightforward to verify that, in the initial limit,

$$\dot{u}(0) = \Delta \tilde{T}.$$

Thus, with high rate data for the vessel speed u and the propeller speed δn, and using a Savitsky-Golay filter to determine the acceleration $\dot{u}$, one obtains a collection of initial accelerations corresponding to step inputs in throttle. Recalling the thrust relation (23) and applying the pseudoinverse, one obtains a least-squares error solution to the overdetermined linear algebraic system for $\tilde{c}$ and $\tilde{d}$. Experimental identification results for the Ribcraft USV verify that $\tilde{c}$ and $\tilde{d}$ do not vary with the nominal speed, even in planing mode, so that $\tilde{T}$ differs from T by a constant scale factor. This scale factor can be absorbed into the input parameters of the speed and steering models in Sections 2.3.1 and 2.3.2, so that one seeks to identify $\tilde{T}$ rather than T.

3.2.2. Remaining State Space Model Parameters

Referring to Eq. (19), suppose we have obtained sampled data for a state history $\boldsymbol{x}(t)$ and, using the Savitsky-Golay algorithm, the corresponding state rate history $\dot{\boldsymbol{x}}(t)$ in response to some suitably rich input history $\boldsymbol{u}(t)$. These data define a system of algebraic equations for the parameters appearing in $\boldsymbol{A}$ and $\boldsymbol{B}$. At each of the N sample times t_i, for $i \in \{1, \ldots, N\}$, one has

$$\dot{\boldsymbol{x}}(t_i) = \boldsymbol{A}\boldsymbol{x}(t_i) + \boldsymbol{B}\boldsymbol{u}(t_i) + \boldsymbol{B}_{\text{bias}}.$$

Incorporating the steady-state constraints (20) and (21) by substituting

$$\boldsymbol{B} = -\boldsymbol{A}\boldsymbol{\Phi} \qquad \text{and} \qquad \boldsymbol{B}_{\text{bias}} = -\boldsymbol{A}\boldsymbol{\Phi}_{\text{bias}}$$

gives nN equations

$$\dot{\boldsymbol{x}}(t_i) = \boldsymbol{A}\left(\boldsymbol{x}(t_i) - \boldsymbol{\Phi}\boldsymbol{u}(t_i) - \boldsymbol{\Phi}_{\text{bias}}\right) \tag{25}$$

for the n^2 parameters of $\boldsymbol{A}$. A least-squares estimate for these parameters can be obtained using the pseudoinverse (Stengel, 1986) for $N > n$. Of course, the absolute accuracy of the estimate depends on the system structure and the data quality. An input history that excites all of the dynamic modes will yield much better parameter estimates, as can be verified using independent validation data.

3.3. Model Identification Results

Field trials for the riverine USV were performed in order to compare various models. Section 3.3.1 describes an experimentally obtained steady-state map that relates the fixed values of throttle, propeller speed, and thrust angle to steady turn rate, forward velocity, and side velocity. Actuator dynamics, found by applying step thrust angle commands while recording the actual thrust angle and by sending step throttle commands while recording propeller speed, are discussed in Section 3.3.2. Section 3.3.3 shows parameter fits for the thruster model. Section 3.3.4 presents simplified vehicle dynamic models deduced from closed-loop field trials involving commanding square waves in heading and velocity while recording time histories of thrust angle, propeller speed, orientation, and velocity.

3.3.1. Steady-State Input/Output Relationships

To obtain steady-state motion data, sweeps of discrete steering angles at discrete throttle settings were performed. Steady-state motion data for the Ribcraft USV are given in Figure 4 for two of the eight forward speeds at which steady motion data were collected. The vessel's throttle exhibits a deadband from −20% to roughly 35%. For identification purposes, throttle settings ranged from 35% to 65%, providing data on the transition from the dead band region into the semidisplacement and planing region. Thrust angles ranged from -30° to 30°.

Linear fits to the steady-state motion data result in the following models for steady turn rate (in deg/s), sideslip angle (in degrees), and sideslip velocity (in m/s):

$$\begin{aligned} r_{\text{ss}} &= K_r \, \delta s_{\text{ss}} + K_{r_{\text{bias}}}, \\ \beta_{\text{ss}} &= K_\beta r_{\text{ss}} + K_{\beta_{\text{bias}}}, \\ v_{\text{ss}} &= K_v \, \delta s_{\text{ss}} + K_{v_{\text{bias}}}, \end{aligned}$$

where the steering angle δs_{ss} is specified in degrees.

Values for these parameters are given in Table I. Examining these data, one finds that the steady turn rate due to a nonzero steering angle increases with throttle setting. The variation in sideslip angle and side velocity with steering angle decreases in the semidisplacement region (throttle

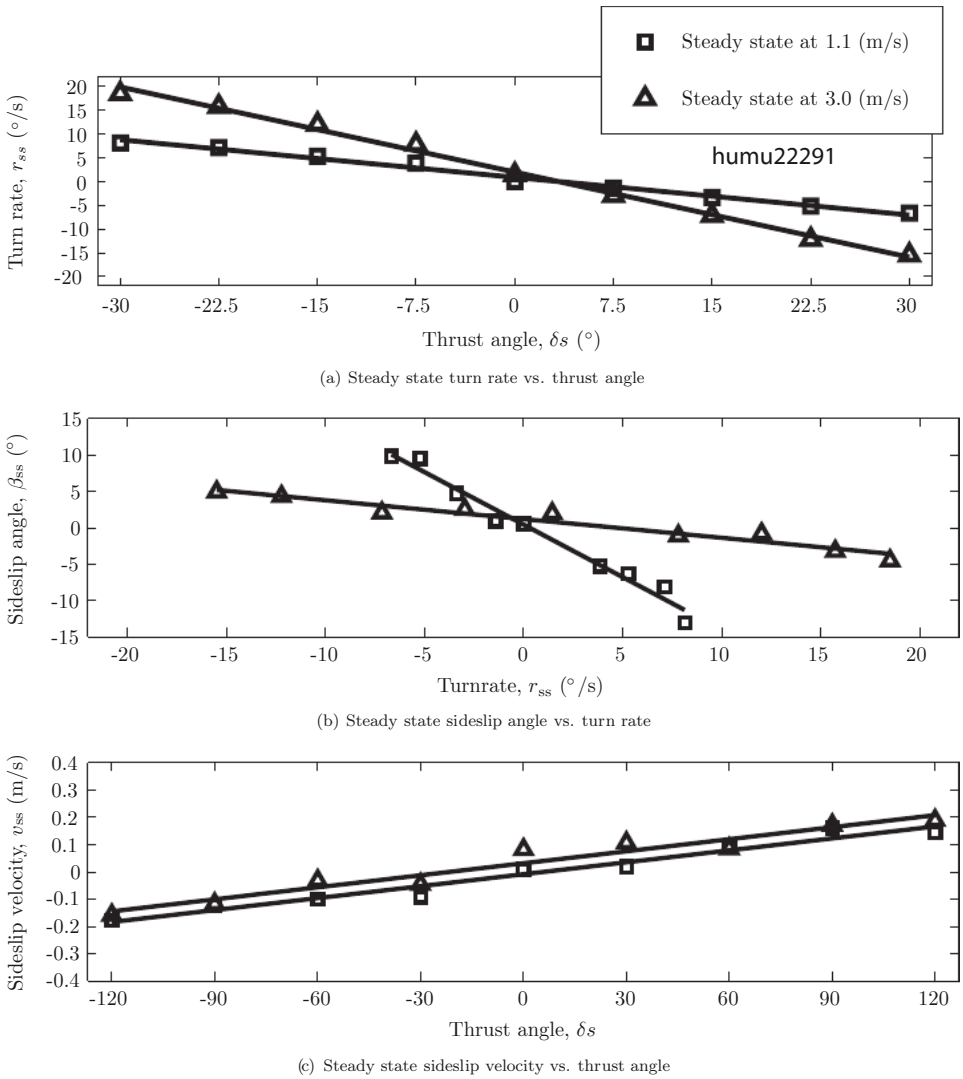

(a) Steady state turn rate vs. thrust angle

(b) Steady state sideslip angle vs. turn rate

(c) Steady state sideslip velocity vs. thrust angle

Figure 4. Selected steady-state turn rate and sideslip date for the Ribcraft USV. Data were collected for eight forward speeds, from 1.1 to 9.2 m/s.

Table I. DC gains of β, v, and r for the Ribcraft USV. (Parameter units suppressed.)

Forward speed (m/s)	K_β	$K_{\beta_{\text{bias}}}$	K_v	$K_{v_{\text{bias}}}$	K_r	$K_{r_{\text{bias}}}$
1.1	−1.44	0.44	0.0060	−0.009	−0.28	0.87
1.5	−1.36	0.62	0.0056	−0.004	−0.28	0.84
2.6	−0.26	1.20	0.0060	0.031	−0.60	1.97
3.0	−0.13	0.71	0.0040	0.021	−0.68	2.11
3.2	0.00	1.08	−0.0000	0.056	−0.76	2.02
4.0	0.08	1.17	−0.0036	0.080	−0.76	2.03
7.6	−0.10	1.22	0.0096	0.135	−0.76	2.28
9.2	−0.12	1.11	0.0120	0.122	−0.76	2.21

values of 45%, 50%, and 55%), but at low throttle settings, large sideslip angles occur during steady turns.

Figure 5 shows steady forward speeds versus propeller speed for $\delta s = 0^\circ$ with polynomial fits for the reverse, displacement, semidisplacement, and planing modes. Note that Froude numbers of 0.45 and 1 (corresponding to speeds of 3.1 and 7 m/s) define the boundaries between the forward velocity modes.

Note that steering angle sweeps were also performed for reverse throttle settings to obtain steady-state steering data for backward motion. An unstable equilibrium at zero turn rate causes the vessel, unassisted by feedback control, to fall into a left or right turn. Once established in this turning motion, transition to an opposing turn must overcome

15564967, 2013, 30, Downloaded from https://onlinelibrary.wiley.com. By Universita Di Pavia- on [25/11/2021]. Re-use and distribution is strictly not permitted, except for Open Access articles

15564967, 2013, 30, Downloaded from https://onlinelibrary.wiley.com. By Universita Di Pavia- on [25/11/2021]. Re-use and distribution is strictly not permitted, except for Open Access articles

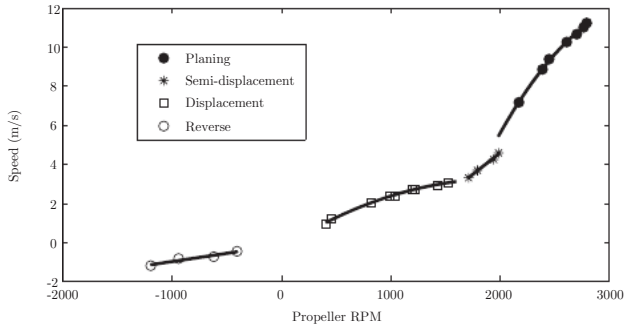

Figure 5. Steady-state speed fits.

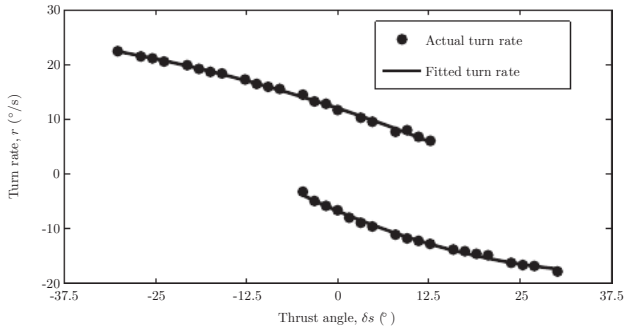

Figure 6. Steady-state backwards turn rate fit.

the previous turning condition's region of attraction, requiring considerable control effort. We note that motion planning and trajectory tracking algorithms for reverse motion must account for this phenomenon in order to avoid saturation and ensure adequate performance; see Gadre et al. (2012b).

In reverse motion, there is a bifurcation in the steady-state turn rate, resulting in stable left and right turn motions; see Figure 6. Because the vessel speed in reverse gear does not vary greatly, the parameters defining a steady turn model for reverse motion do not vary with speed. The variation in steady turn rate (in deg/s) with thrust angle (in degrees) is well-modeled using a quadratic fit:

Reverse turn to port:

$$r_{ss} = -0.0032\delta s^2 - 0.4428\delta s + 11.99525,$$

Reverse turn to starboard:

$$r_{ss} = 0.0072\delta s^2 - 0.5684\delta s - 6.77138.$$

Taking reverse speed and thrust angle as bifurcation parameters, one finds a pitchfork bifurcation at zero thrust angle that degenerates into a saddle-node bifurcation when the thrust angle is offset.

3.3.2. Actuator Nonlinearities

The propulsion and steering assemblies impose physical constraints on propeller speed and thrust angle adjustments. The Ribcraft USV's steering angle is limited such that $|\delta s| \leq 30^\circ$. The thruster's angular rate saturates at roughly ± 15 deg/s due to limitations of the hydraulic motor that moves the gimbaled thruster assembly. The thrust angle is tightly controlled by a PID controller when reference commands satisfy these magnitude and rate limits. The throttle commands the manifold pressure in the engine with a delay of roughly 0.5 s. Changing gear (forward, neutral, or reverse) gives an additional 1.5 s delay. Furthermore, the steady-state relationship between throttle position and manifold pressure is nonlinear. Because the manifold pressure and engine dynamics are not measured or estimated, we characterize the steady-state relationship between throttle setting and propeller speed. Throttle is measured in percent, with a deadband from -20% to 35%. The engine has hysteresis in the displacement speed region, as can be observed in Figure 7. One might expect hysteresis in the throttle/forward speed relationship when passing between the semi-displacement and planing modes, but none is evident. Hysteresis is only apparent in the throttle/propeller speed relationship; see Figures 5 and 7. The following data fits for reverse, displacement/semidisplacement, and planing modes are shown in Figure 7:

$$\delta T = 0.0368\delta n - 12.88, \tag{26}$$

$$\delta T = 4.08 \times 10^{-5}\delta n|\delta n| - 0.0108\delta n + 37.08, \tag{27}$$

$$\delta T = 0.0656\delta n - 11.41. \tag{28}$$

These fits define the steady-state relationship between throttle setting (in percent) and propeller speed (in RPM) outside the deadband region; the fits are used to define a feedforward term in the engine speed controller that mitigates hysteresis effects.

3.3.3. Thruster Model

To extract $\tilde{c}$ and $\tilde{d}$ from Eq. (23), experimental throttle step responses were obtained, with measurements of velocity, acceleration, and propeller speed. Figure 8 shows a fit of $\tilde{c}$ and $\tilde{d}$. The thrust fit matches the data well, yielding parameter values $\tilde{c} = -1.42 \times 10^{-4}$ ($s^{-1}RPM^{-1}$) and $\tilde{d} = 8.96 \times 10^{-7}$ (ms^{-2} RPM^{-2}).

3.3.4. Speed and Steering Dynamic Parameters

Figures 9, 10, and 11 show representative time histories (actual and simulated) of u, r, and β for the feedback controlled Ribcraft USV in response to commanded square waves in heading and speed. These plots use validation data sets, obtained independently of the data used for model identification. Examining Figure 9, it is clear that the first-order linear

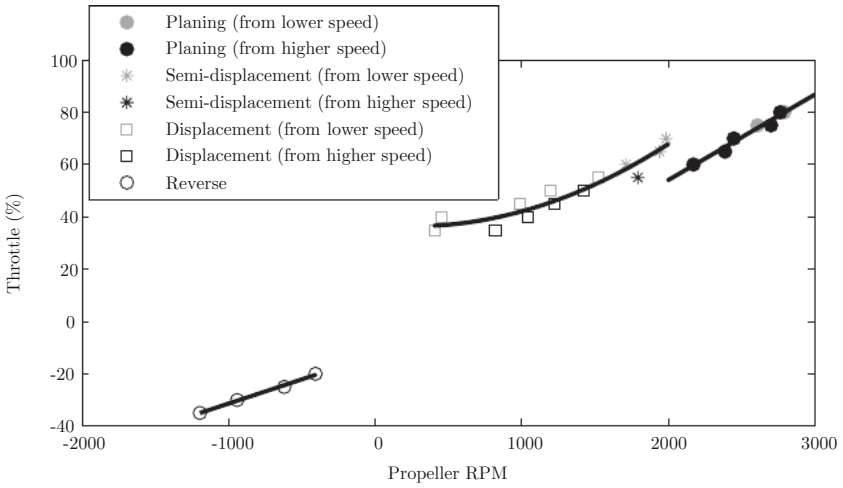

Figure 7. Steady-state throttle fits.

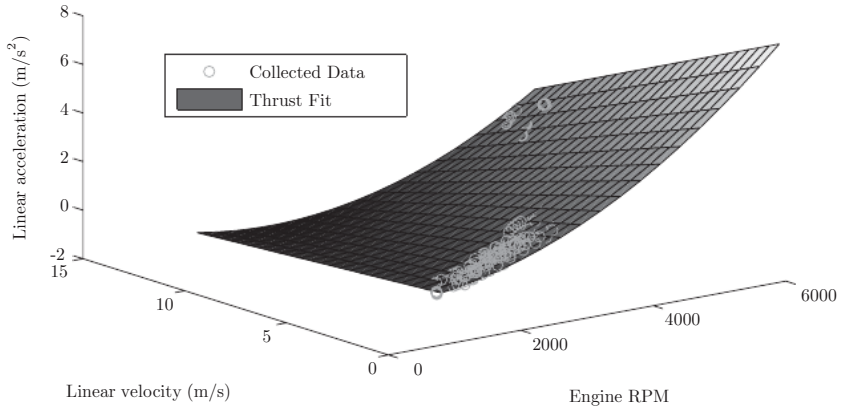

Figure 8. Thrust parameter fitting.

speed model identified for this displacement speed range captures the behavior of the vehicle in surge. For the data shown in Figures 10 and 11, the Nomoto model with sideslip and the linear model best approximate the true course angle history when the boat is moving at low speeds. This observation illustrates the need to account for sideslip dynamics at low speeds, when the vessel is operating in displacement mode.

Table II shows parameter identification cost function values for identified models of the Ribcraft USV steering dynamics. These values were computed using the same validation data sets used in Figures 9, 10, and 11. Time histories of estimated turn rate and sideslip angle are calculated using steering model parameters and actual thrust angle time histories taken from validation data. The cost function

$$J = \sqrt{\frac{1}{t_{\text{total}}}\sum_{i=1}^{N}[\beta_{\text{est}}(i) - \beta_{\text{val}}(i)]^2} + \sqrt{\frac{1}{t_{\text{total}}}\sum_{i=1}^{N}[r_{\text{est}}(i) - r_{\text{val}}(i)]^2} \quad (29)$$

provides a comparison between estimated turn rate and sideslip and actual turn rate and sideslip (from the validation data). The parameter t_{total} is the total time of the time

15564967, 2013, 30, Downloaded from https://onlinelibrary.wiley.com. By Universita Di Pavia- on [25/11/2021]. Re-use and distribution is strictly not permitted, except for Open Access articles

15564967, 2013, 30, Downloaded from https://onlinelibrary.wiley.com. By Universita Di Pavia- on [25/11/2021]. Re-use and distribution is strictly not permitted, except for Open Access articles

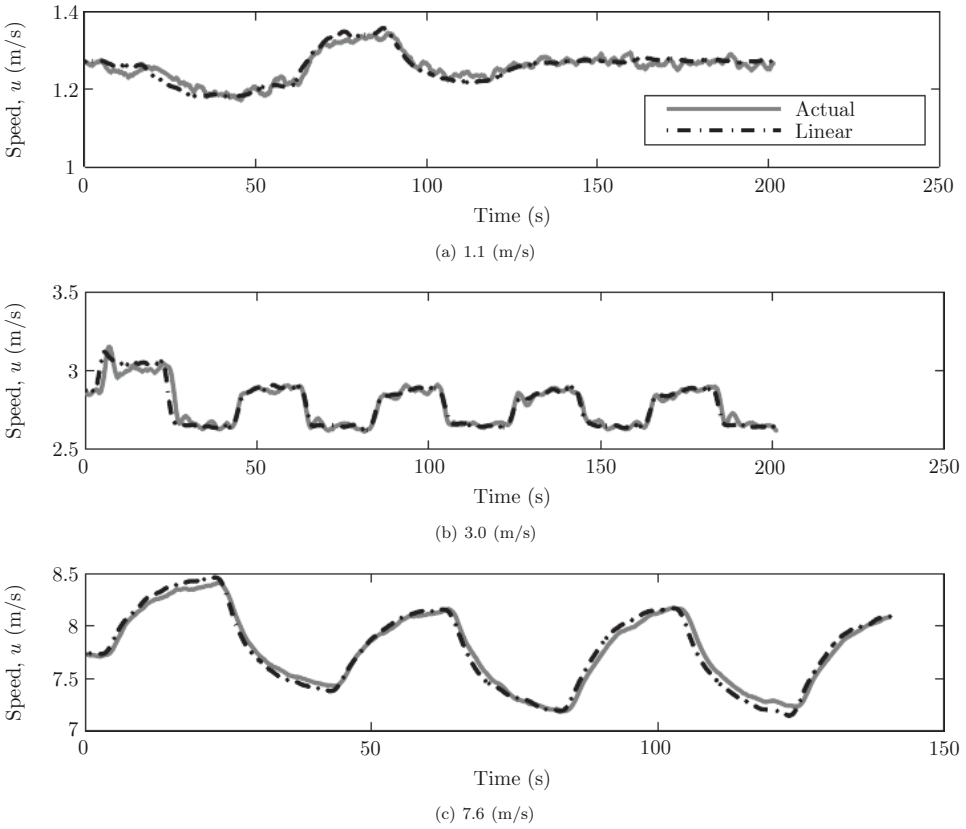

Figure 9. Measured forward speed vs. simulated forward speed for a range of forward speeds.

histories. State variables with the subscript "val" denote validation data, while state variables with the subscript "est" denote estimates obtained using model parameters. Note that the asterisks in Table II (at speeds of 2.6, 3.0, and 3.2 m/s) indicate that the model parameters result in unstable systems that yield unreasonable cost function values.

The steady-state sideslip angle decreases nearly to zero for some displacement and semidisplacement speed regions, so the sideslip angle dynamics may not be sufficiently excited to overcome signal noise. In these cases, the parameter identification method, which uses a filtered derivative of state measurements, results in unstable models.

It is unsurprising that the linear steering model performs well at low speeds, since this model has the most parameters. The Nomoto-with-sideslip model performs comparably, however, and requires fewer parameters. Because the sideslip angle remains quite small during maneuvers at higher speeds, one may justifiably adopt the Nomoto steering model in this speed region.

Examining Table II, one finds that it is reasonable to use the Nomoto-with-sideslip model at speeds below 2.6 m/s and to use the simpler Nomoto model at higher speeds. Table III shows the parameter values corresponding to the steering model adopted for the given reference speed. [Data fits for the three steering models over the full speed range can be found in Sonnenburg and Woolsey (2010).] Combined with the the first-order linear speed model (14) and the bilinear thrust model (7), this multiple-model representation for the steering dynamics enables one to generate dynamically feasible reference trajectories for the Ribcraft USV. The resulting trajectories may then be tracked using algorithms developed in Section 4.

4. TRAJECTORY TRACKING

Two trajectory controllers are formulated to control a riverine USV whose dynamics are approximated using the speed and steering models obtained in Section 3. First, the problem of tracking a reference trajectory is formulated by defining tracking error dynamics. (Note that the generation of these reference trajectories is not a focus of this paper.) Next, we develop a cascade of PD controllers whose inputs are the reference heading and speed signals, modified based on the tracking error. As an alternative to the PD cascade,

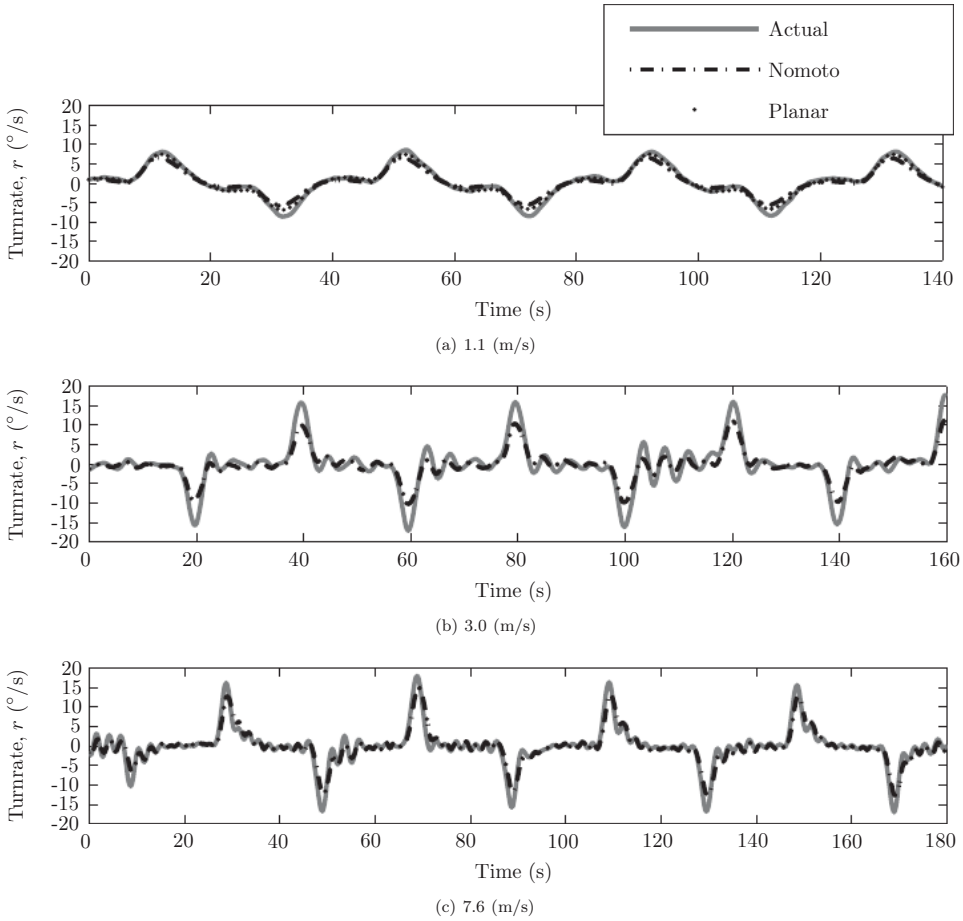

Figure 10. Actual and simulated turn rate time histories for a range of forward speeds.

we describe a nonlinear tracking control law derived using backstepping. The "inner loop" of the backstepping control law is based on the results in Jiang and Nijmeijer (1997) and Jiang et al. (2001). Both control laws are implemented on the Ribcraft USV, and the experimental results are compared.

4.1. Problem Formulation

The planar kinematic equations for a vessel moving in still water are given in Eq. (3). The speed and steering dynamics are estimated using the Nomoto model with sideslip,[1] the linear speed model, and the assumption that $V \approx u$:

$$\dot{u} = a_u u + \tilde{T} + b_{u_{\text{bias}}}, \tag{30}$$

[1]At higher speeds, where the sideslip dynamic model becomes unnecessary, the simpler Nomoto steering model is adopted.

$$\begin{pmatrix} \dot{\beta} \\ \dot{\psi} \\ \dot{r} \end{pmatrix} = \begin{pmatrix} a_\beta & 0 & b_\beta \\ 0 & 0 & 1 \\ 0 & 0 & a_r \end{pmatrix} \begin{pmatrix} \beta \\ \psi \\ r \end{pmatrix} + \begin{pmatrix} 0 \\ 0 \\ b_r \end{pmatrix} \tilde{T}\delta s + \begin{pmatrix} b_{\beta_{\text{bias}}} \\ 0 \\ b_{r_{\text{bias}}} \end{pmatrix}, \tag{31}$$

where $\tilde{T}$ is given by Eq. (23).

To simplify controller development, we recast the dynamics (31) in terms of ψ, r, and χ, giving

$$\begin{pmatrix} \dot{\chi} \\ \dot{\psi} \\ \dot{r} \end{pmatrix} = \begin{pmatrix} a_\beta & -a_\beta & 1+b_\beta \\ 0 & 0 & 1 \\ 0 & 0 & a_r \end{pmatrix} \begin{pmatrix} \chi \\ \psi \\ r \end{pmatrix} + \begin{pmatrix} 0 \\ 0 \\ b_r \end{pmatrix} \tilde{T}\delta s + \begin{pmatrix} b_{\beta_{\text{bias}}} \\ 0 \\ b_{r_{\text{bias}}} \end{pmatrix} \tag{32}$$

with eigenvalues of a_β, 0, and a_r.

Assume a reference trajectory has been generated based upon an initial state and reference thrust angle and propeller

15564967, 2013, 30, Downloaded from https://onlinelibrary.wiley.com. By Universita Di Pavia- on [25/11/2021]. Re-use and distribution is strictly not permitted, except for Open Access articles

15564967, 2013, 30, Downloaded from https://onlinelibrary.wiley.com. By Universita Di Pavia- on [25/11/2021]. Re-use and distribution is strictly not permitted, except for Open Access articles

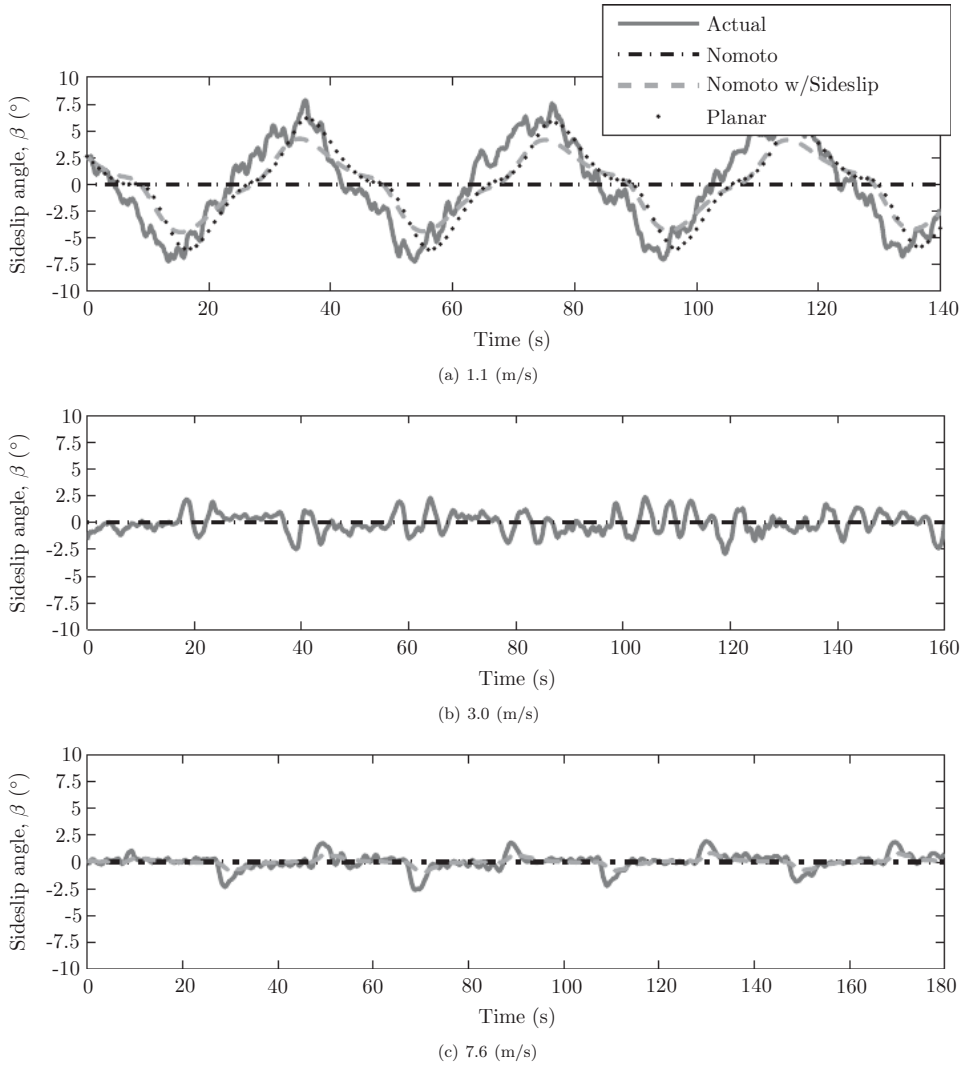

Figure 11. Actual vs. simulated sideslip angle time histories for a range of forward speeds.

speed inputs. Specifically,

$$\dot{x}_{\mathrm{r}} = u_{\mathrm{r}} \sin \chi_{\mathrm{r}},$$

$$\dot{y}_{\mathrm{r}} = u_{\mathrm{r}} \cos \chi_{\mathrm{r}},$$

$$\begin{pmatrix} \dot{\chi}_{\mathrm{r}} \\ \dot{\psi}_{\mathrm{r}} \\ \dot{r}_{\mathrm{r}} \end{pmatrix} = \begin{pmatrix} a_\beta & -a_\beta & 1+b_\beta \\ 0 & 0 & 1 \\ 0 & 0 & a_r \end{pmatrix} \begin{pmatrix} \chi_{\mathrm{r}} \\ \psi_{\mathrm{r}} \\ r_{\mathrm{r}} \end{pmatrix} + \begin{pmatrix} 0 \\ 0 \\ b_r \end{pmatrix} \tilde{T}_r \delta s_{\mathrm{r}} + \begin{pmatrix} b_{\beta_{\mathrm{bias}}} \\ 0 \\ b_{r_{\mathrm{bias}}} \end{pmatrix},$$

$$\dot{u}_{\mathrm{r}} = a_u u_{\mathrm{r}} + \tilde{T}_{\mathrm{r}} + b_{u_{\mathrm{bias}}}.$$

(Since we have assumed that $V \approx u$, in normal operation, we also require that $V_{\mathrm{r}} \approx u_{\mathrm{r}}$.) The trajectory tracking error is

$$\begin{pmatrix} e_s \\ e_y \end{pmatrix} = \begin{pmatrix} \cos\chi & \sin\chi \\ -\sin\chi & \cos\chi \end{pmatrix} \begin{pmatrix} x_{\mathrm{r}} - x \\ y_{\mathrm{r}} - y \end{pmatrix}, \tag{33}$$

$$e_u = u_{\mathrm{r}} - u, \tag{34}$$

$$e_\chi = \chi_{\mathrm{r}} - \chi, \tag{35}$$

$$e_\psi = \psi_{\mathrm{r}} - \psi, \tag{36}$$

$$\dot{e}_\psi = r_{\mathrm{r}} - r. \tag{37}$$

15564967, 2013, 30, Downloaded from https://onlinelibrary.wiley.com. By Universita Di Pavia- on [25/11/2021]. Re-use and distribution is strictly not permitted, except for Open Access articles

Table II. Steering model cost function values.

Forward Speed, (m/s)	Nomoto	Nomoto w/Sideslip	Linear
1.1	5.5	3.6	2.7
1.5	2.5	1.9	2.3
2.6	1.9	1.9	*
3.0	1.4	1.4	*
3.2	0.8	0.9	*
4.0	0.4	0.4	0.7
7.6	0.3	0.3	0.3
9.2	0.5	0.5	0.4

Differentiating the error variables gives

$$\dot{e}_s = [\dot{\chi}_r - a_\beta e_\chi + a_\beta e_\psi - (1+b_\beta)\dot{e}_\psi]e_y - u_r + e_u + u_r \cos e_\chi, \quad (38)$$

$$\dot{e}_y = -[\dot{\chi}_r - a_\beta e_\chi + a_\beta e_\psi - (1+b_\beta)\dot{e}_\psi]e_s + u_r \sin e_\chi, \quad (39)$$

$$\dot{e}_u = a_u e_u + \tilde{T}_r - \tilde{T}, \quad (40)$$

$$\begin{pmatrix} \dot{e}_\chi \\ \dot{e}_\psi \\ \ddot{e}_\psi \end{pmatrix} = \begin{pmatrix} a_\beta & -a_\beta & 1+b_\beta \\ 0 & 0 & 1 \\ 0 & 0 & a_r \end{pmatrix} \begin{pmatrix} e_\chi \\ e_\psi \\ \dot{e}_\psi \end{pmatrix} + \begin{pmatrix} 0 \\ 0 \\ b_r \end{pmatrix} (\tilde{T}_r \delta s_r - \tilde{T}\delta s). \quad (41)$$

Figure 12 shows all of the state components, as well as the reference state, and the along track and cross track errors.

4.2. Cascaded PD Control

A simple closed-loop controller incorporating a series of proportional and PD controllers is presented here. The cross track and along track error terms are used to adjust the reference speed and heading such that the vessel converges to the correct reference position. Define the speed and heading corrections

$$u_{\text{corr}} = k_{p_s} e_s, \quad (42)$$

$$\psi_{\text{corr}} = k_{p_y} e_y. \quad (43)$$

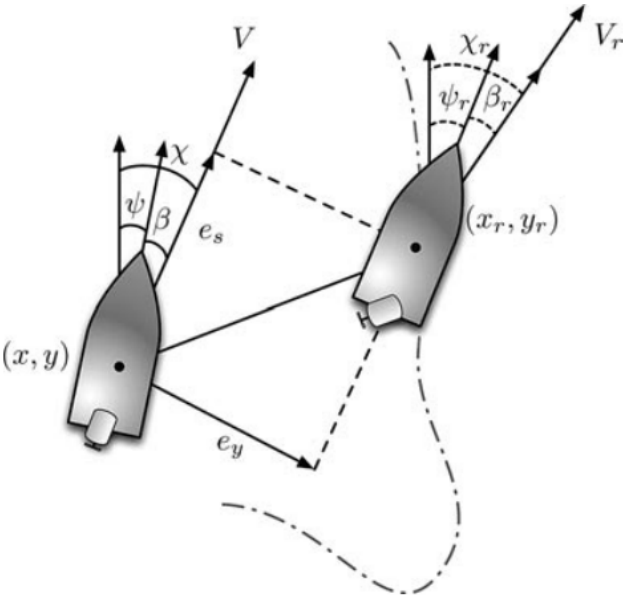

Figure 12. Notation and formulation of cross track and along track error.

To establish a speed and heading that drive the vessel toward the desired trajectory, we define the following propeller speed and thrust angle commands:

$$\delta n = \delta n_r + k_{p_u}(u_{\text{corr}} + e_u) + k_{d_u}(\dot{u}_{\text{corr}} + \dot{e}_u), \quad (44)$$

$$\delta s = \delta s_r + k_{p_\psi}(\psi_{\text{corr}} + e_\psi) + k_{d_\psi}(\dot{\psi}_{\text{corr}} + \dot{e}_\psi), \quad (45)$$

The control structure can be seen in Figure 13.

The closed-loop error dynamics are

$$\dot{e}_s = [\dot{\chi}_r - a_\beta e_\chi + a_\beta e_\psi - (1+b_\beta)\dot{e}_\psi]e_y - u_r + e_u + u_r \cos e_\chi, \quad (46)$$

$$\dot{e}_y = -[\dot{\chi}_r - a_\beta e_\chi + a_\beta e_\psi - (1+b_\beta)\dot{e}_\psi]e_s + u_r \sin e_\chi, \quad (47)$$

Table III. Speed and steering model parameter values. (Parameter units suppressed.)

Forward speed (m/s)	a_u	$b_{u_{\text{bias}}}$	a_β	b_β	$b_{\beta_{\text{bias}}}$	a_r	b_r	$b_{r_{\text{bias}}}$
1.1	−0.12	0.07	−0.140	−0.20	0.061	−0.34	−1.06	0.29
1.5	−0.31	0.33	−0.135	−0.10	0.008	−0.40	−1.11	0.77
2.6	−0.58	0.85	0.035	−0.01	0.042	−0.39	−0.33	0.78
3.0	−1.09	2.19	N/A	N/A	N/A	−0.52	−0.30	1.10
3.2	−1.00	1.75	N/A	N/A	N/A	−0.69	−0.33	1.40
4.0	−0.17	−1.12	N/A	N/A	N/A	−1.29	−0.46	2.62
7.6	−0.06	−1.65	N/A	N/A	N/A	−1.08	−0.39	2.47
9.2	−0.10	−1.31	N/A	N/A	N/A	−0.29	−0.10	0.65

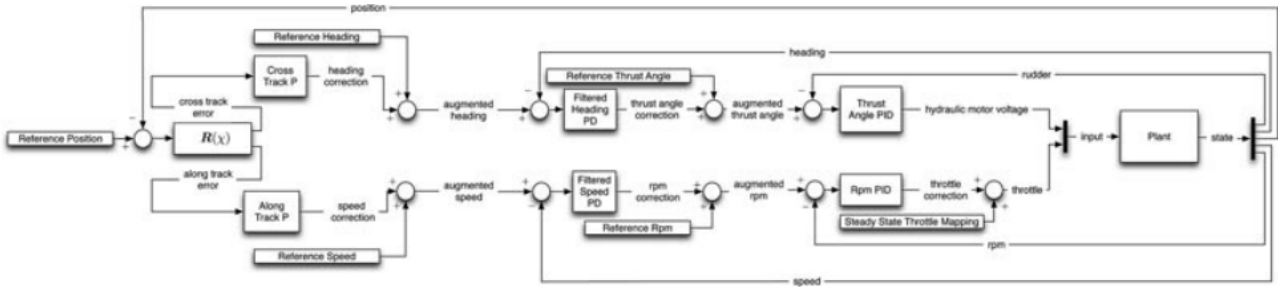

Figure 13. Cascaded trajectory controller.

$$\begin{pmatrix}\dot{e}_\chi\\ \dot{e}_\psi\\ \ddot{e}_\psi\end{pmatrix} = \begin{pmatrix}a_\beta & -a_\beta & 1+b_\beta\\ 0 & 0 & 1\\ 0 & 0 & a_r\end{pmatrix}\begin{pmatrix}e_\chi\\ e_\psi\\ \dot{e}_\psi\end{pmatrix} + \begin{pmatrix}0\\ 0\\ b_r\end{pmatrix} f_\psi(e_s, e_y, e_\chi, e_\psi, e_{\dot\psi}, e_u), \quad (48)$$

$$\dot{e}_u = f_u(e_s, e_y, e_\chi, e_\psi, e_{\dot\psi}, e_u), \quad (49)$$

where the lengthy expressions represented by f_ψ and f_u are given in Appendix A. These error dynamics are nonlinear and time-varying. In the special case in which the reference speed and course rate are constant, however, one may linearize to obtain linear, time-invariant error dynamics. In this case, one may analyze tracking error convergence by computing the eigenvalues of the state matrix, which is given in Eq. (B.1) in Appendix B.

Using parameter values from system identification experiments, and control gains obtained through experimental tuning, one may examine the system eigenvalues for a range of operating conditions. Doing so, with the nominal value $\dot{\chi}_r = 0$, one finds that eigenvalues are in the left half of the complex plane for each throttle setting, indicating that the tracking error dynamics are locally exponentially stable at each such operating condition. Explicit values for control gains and eigenvalues are given in Sonnenburg and Woolsey (2010). Though the constant speed and course rate assumptions are somewhat restrictive, and the results of spectral analysis only hold locally, these stability results can be used to compare the PD cascade approach with the backstepping controller developed in Section 4.3.

4.3. Backstepping

As an alternative to the more conventional PD control approach described in Section 4.2, one may use backstepping to attenuate the error terms e_s, e_y, e_u, e_χ, and e_ψ. Take the adjusted position error to be

$$\begin{pmatrix}e_s\\ e_y\end{pmatrix} = \kappa_5\begin{pmatrix}\cos\chi & \sin\chi\\ -\sin\chi & \cos\chi\end{pmatrix}\begin{pmatrix}x_r - x\\ y_r - y\end{pmatrix},$$

where κ_5 is a constant parameter. (This parameter will ultimately play the role of a turn rate gain in the inner loop of the backstepping controller.)

The rates of change of the along track and cross track error are

$$\begin{pmatrix}\dot{e}_s\\ \dot{e}_y\end{pmatrix} = \begin{pmatrix}\dot{\chi}e_y + \kappa_5(-u_r + e_u + u_r\cos e_\chi)\\ -\dot{\chi}e_s + \kappa_5 u_r \sin e_\chi\end{pmatrix}.$$

We transform and group the tracking error variables as follows:

$$\begin{pmatrix}\boldsymbol{\eta}\\ \hline \boldsymbol{\xi}\\ \hline e_\psi\end{pmatrix} = \begin{pmatrix}\eta_1\\ \eta_2\\ \eta_3\\ \hline \xi_1\\ \xi_2\\ \hline e_\psi\end{pmatrix} = \begin{pmatrix}e_s\\ e_y\\ e_\chi\\ \hline -a_\beta e_\psi + (b_\beta+1)\dot{e}_\psi\\ e_u\\ \hline e_\psi\end{pmatrix}. \quad (50)$$

The error dynamics, in the transformed variables, are

$$\dot{\eta}_1 = (\dot{\chi}_r - a_\beta\eta_3 - \xi_1)\eta_2 + \kappa_5(-u_r + \xi_2 + u_r\cos\eta_3), \quad (51)$$

$$\dot{\eta}_2 = -(\dot{\chi}_r - a_\beta\eta_3 - \xi_1)\eta_1 + \kappa_5 u_r \sin\eta_3, \quad (52)$$

$$\dot{\eta}_3 = a_\beta\eta_3 + \xi_1, \quad (53)$$

$$\dot{\xi}_1 = \frac{a_r(b_\beta+1) - a_\beta}{1+b_\beta}\xi_1 + \frac{(a_r(b_\beta+1) - a_\beta)a_\beta}{1+b_\beta}e_\psi + (b_\beta b_r + b_r)(\tilde{T}_r\,\delta s_r - \tilde{T}\,\delta s), \quad (54)$$

$$\dot{\xi}_2 = a_u\xi_2 + \tilde{T}_r - \tilde{T}, \quad (55)$$

$$\begin{pmatrix}\dot{e}_\psi\\ \ddot{e}_\psi\end{pmatrix} = \begin{pmatrix}0 & 1\\ 0 & a_r\end{pmatrix}\begin{pmatrix}e_\psi\\ \dot{e}_\psi\end{pmatrix} + \begin{pmatrix}0\\ b_r\end{pmatrix}(\tilde{T}_r\delta s_r - \tilde{T}\,\delta s). \quad (56)$$

Following in the spirit of Jiang et al. (2001) and Jiang and Nijmeijer (1997), we define the following virtual inputs $\xi_1 = \phi_1(\eta)$ and $\xi_2 = \phi_2(\eta)$ to stabilize the $\dot{\boldsymbol{\eta}}$ subsystem (51), (52), and (53):

$$\xi_1 = \phi_1(\boldsymbol{\eta}) = -\frac{\sin\eta_3}{\eta_3}\eta_2 u_r\kappa_5 - \kappa_1\tanh(\kappa_2\eta_3) - a_\beta\eta_3, \quad (57)$$

$$\xi_2 = \phi_2(\boldsymbol{\eta}) = u_r - u_r\cos\eta_3 - \kappa_3\tanh(\kappa_4\eta_1), \quad (58)$$

where the parameters κ_1, κ_2, κ_3, κ_4, and κ_5 are positive tuning factors that adjust controller sensitivity and amplitude. The candidate Lyapunov function

$$V_1(\boldsymbol{\eta}) = \frac{1}{2}\eta_1^2 + \frac{1}{2}\eta_2^2 + \frac{1}{2}\eta_3^2$$

15564967, 2013, 30, Downloaded from https://onlinelibrary.wiley.com. By Universita Di Pavia- on [25/11/2021]. Re-use and distribution is strictly not permitted, except for Open Access articles

15564967, 2013, 30, Downloaded from https://onlinelibrary.wiley.com. By Universita Di Pavia- on [25/11/2021]. Re-use and distribution is strictly not permitted, except for Open Access articles

is positive definite (Khalil, 2002). The derivative of the candidate Lyapunov function is

$$\begin{aligned}\dot{V}_1 &= \eta_1\dot{\eta}_1 + \eta_2\dot{\eta}_2 + \eta_3\dot{\eta}_3 \\ &= \eta_1[(\dot{\chi}_r - a_\beta\eta_3 - \xi_1)\eta_2 - \kappa_5(u_r - \xi_2 - u_r\cos\eta_3)] \\ &\quad + \eta_2[-(\dot{\chi}_r - a_\beta\eta_3 - \xi_1)\eta_1 + \kappa_5 u_r\sin\eta_3] \\ &\quad + \eta_3(a_\beta\eta_3 + \xi_1) \\ &= -\kappa_3\kappa_5\eta_1\tanh(\kappa_4\eta_1) + \eta_1\eta_2(\dot{\chi}_r - a_\beta\eta_3 - \xi_1) \\ &\quad - \eta_1\eta_2(\dot{\chi}_r - a_\beta\eta_3 - \xi_1) + \kappa_5\eta_2 u_r\sin\eta_3 \\ &\quad + \eta_3\left(-\frac{\sin\eta_3}{\eta_3}\kappa_5\eta_2 u_r - \kappa_1\tanh(\kappa_2\eta_3)\right) \\ &= -\kappa_3\kappa_5\eta_1\tanh(\kappa_4\eta_1) - \kappa_1\eta_3\tanh(\kappa_2\eta_3) \le 0.\end{aligned}$$

Lemma 4.1. *Assume that χ_r and u_r are bounded. Also, assume that $u_r(t) \neq 0$ on $[0,\infty)$. All trajectories of Eqs. (51), (52), and (53) with inputs defined by Eqs. (57) and (58) are globally uniformly bounded and*

$$\lim_{t\to\infty}|\boldsymbol{\eta}| = 0.$$

Proof: Since the candidate Lyapunov function is positive definite and radially unbounded and the candidate Lyapunov function's derivative is negative semidefinite, $\boldsymbol{\eta}$ is uniformly bounded and defined for $t \ge 0$. Note that the Lyapunov function's second derivative is bounded. By Barbalat's lemma, η_1 and η_3 converge to zero. To prove that η_2 converges to zero, note that $\eta_3 \to 0$ as $t \to \infty$ and

$$\frac{\sin\theta}{\theta} = \int_0^1 \cos(s\theta)ds$$

so $\int_0^1\cos(s\eta_3)ds \to 1$ as $t\to\infty$. Recall that $u_r(t)\neq 0$ for all $t \ge 0$. The η_3 dynamics of the closed-loop system are

$$\dot{\eta}_3 = -\kappa_1\tanh(\kappa_2\eta_3) + \kappa_5\eta_2 u_r\int_0^1\cos(s\eta_3)ds.$$

Note that η_3 tends to 0 so $\eta_2 u_r\int_0^1\cos(s\eta_3)ds$ must go to 0, which implies that $\eta_2 \to 0$. □

Lemma 4.2. *The equilibrium state $\boldsymbol{\eta} = \mathbf{0}$ for the system (51)–(53) under the feedback control law (57) and (58) is exponentially stable for continuous and bounded $u_r \neq 0$ and $\dot{\chi}_r$.*

Proof: The linearized closed-loop system around the equilibrium point is

$$\dot{\boldsymbol{\eta}} = \begin{pmatrix} -\kappa_3\kappa_4\kappa_5 & \dot{\chi}_r & 0 \\ -\dot{\chi}_r & 0 & \kappa_5 u_r \\ 0 & -\kappa_5 u_r & -\kappa_1\kappa_2 \end{pmatrix}\boldsymbol{\eta}. \tag{59}$$

The system (59) is exponentially stable if

$$\boldsymbol{P}\boldsymbol{A}(t) + \boldsymbol{A}^T(t)\boldsymbol{P} = -\boldsymbol{Q}(t), \tag{60}$$

where $\boldsymbol{P}$ and $\boldsymbol{Q}(t)$ are positive definite symmetric matrices. Define a constant, positive definite matrix

$$\boldsymbol{P} = \begin{pmatrix} p_1 & 0 & 0 \\ 0 & p_2 & p_3 \\ 0 & p_3 & p_4 \end{pmatrix}.$$

From Eq. (60), we have

$$\boldsymbol{Q}(t) = \begin{pmatrix} 2p_1\kappa_3\kappa_4\kappa_5 & -\dot{\chi}_r(p_1 - p_2) & \dot{\chi}_r p_3 \\ -\dot{\chi}_r(p_1 - p_2) & 2p_3 u_r\kappa_5 & (p_4 - p_2)u_r\kappa_5 - p_3\kappa_1\kappa_2 \\ \dot{\chi}_r p_3 & (p_4 - p_2)u_r\kappa_5 - p_3\kappa_1\kappa_2 & 2p_4\kappa_1\kappa_2 - 2u_r\kappa_5 p_3 \end{pmatrix}.$$

To simplify analysis, set $p_1 = p_2$ and $p_3 = \frac{p_1 - p_4}{\mathrm{sgn}(u_r)}$. Then

$$\boldsymbol{Q}(t) = \begin{pmatrix} 2p_1\kappa_3\kappa_4\kappa_5 & 0 & \frac{\dot{\chi}_r(t)(p_1 - p_4)}{\mathrm{sgn}(u_r)} \\ 0 & 2(p_1 - p_4)|u_r(t)|\kappa_5 & 0 \\ \frac{\dot{\chi}_r(t)(p_1 - p_4)}{\mathrm{sgn}(u_r)} & 0 & 2p_4\kappa_1\kappa_2 - 2|u_r(t)|\kappa_5(p_1 - p_4) \end{pmatrix}.$$

The matrix $\boldsymbol{Q}(t)$ is positive definite provided the leading principal minors are positive. Setting $p_4 > 0$ and $p_1 = p_4 + \epsilon$ where $\epsilon > 0$ is arbitrarily small, the leading principal minors are

$$\begin{aligned} &2p_1\kappa_3\kappa_4\kappa_5 > 0, \\ &4p_1 p_3|u_r|\kappa_3\kappa_4\kappa_5^2 > 0, \\ &\quad -2\dot{\chi}_r^2\kappa_5(p_1 - p_4)^3|u_r| + 8\kappa_1\kappa_2\kappa_3\kappa_4\kappa_5^2 p_1(p_1 - p_4)p_4|u_r| \\ &\quad - 8\kappa_3\kappa_4\kappa_5^3 p_1(p_1 - p_4)^2 u_r^2 > 0. \end{aligned}$$

Thus, by Lyapunov's indirect method, the time-varying closed-loop system (51)–(53), with feedback control law (57) and (58), is locally exponentially stable. □

Setting the inputs to

$$\begin{aligned}\begin{pmatrix}\tilde{T}\delta s \\ \tilde{T}\end{pmatrix} &= \begin{pmatrix}\tilde{T}_r\delta s_r \\ \tilde{T}_r\end{pmatrix} + \begin{pmatrix}\frac{1}{b_r(b_\beta+1)} & 0 \\ 0 & 1\end{pmatrix}\left[\begin{pmatrix}\frac{a_r(b_\beta+1)-a_\beta}{1+b_\beta}\xi_1 + \frac{(a_r(b_\beta+1)-a_\beta)a_\beta}{1+b_\beta}e_\psi \\ a_u\xi_2\end{pmatrix} - \begin{pmatrix}\left\{-\left[\int_0^1\cos(s\eta_3)ds\right]\kappa_5 u_r\right\}[-(\dot{\chi}_r - a_\beta\eta_3 + \xi_1)\eta_1 + \kappa_5 u_r\sin\eta_3] \\ -\kappa_3\kappa_4\mathrm{sech}^2(\kappa_4\eta_1)[(\dot{\chi}_r - a_\beta\eta_3 + \xi_1)\eta_2 + \kappa_5(-u_r + u_r\cos\eta_3 + \xi_2)]\end{pmatrix}\right. \\ &\quad - \begin{pmatrix}\left\{-\left[\int_0^1\sin(s\eta_3)sds\right]\eta_2\kappa_5 u_r - \kappa_1\kappa_2\mathrm{sech}^2(\kappa_2\eta_3) - a_\beta\right\}(a_\beta\eta_3 + \xi_1) \\ u_r\sin\eta_3(a_\beta\eta_3 + \xi_1)\end{pmatrix} + \begin{pmatrix}\eta_3 \\ \eta_1\end{pmatrix} \\ &\quad \left. + \boldsymbol{K}\begin{pmatrix}\xi_1 + \left[\int_0^1\cos(s\eta_3)ds\right]\eta_2\kappa_5 u_r + \kappa_1\tanh(\kappa_2\eta_3) + a_\beta\eta_3 \\ \xi_2 - u_r + u_r\cos\eta_3 + \kappa_3\tanh(\kappa_4\eta_1)\end{pmatrix}\right]\end{aligned} \tag{61}$$

15564967, 2013, 30, Downloaded from https://onlinelibrary.wiley.com. By Universita Di Pavia- on [25/11/2021]. Re-use and distribution is strictly not permitted, except for Open Access articles

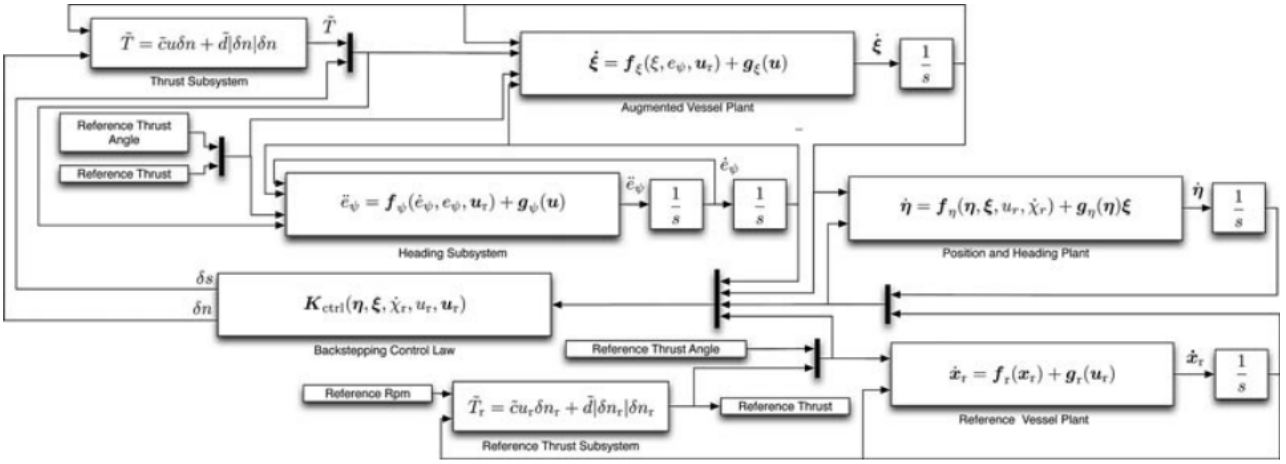

Figure 14. Backstepping feedback system.

asymptotically stabilizes the equilibrium $\boldsymbol{\eta} = \boldsymbol{0}$ and $\boldsymbol{\xi} = \boldsymbol{0}$ if β_r, χ_r, δs_r, u_r, and δn_r are bounded, the matrix

$$\boldsymbol{K} = \begin{pmatrix} k_1 & k_2 \\ k_2 & k_3 \end{pmatrix}$$

is positive definite, and $\tilde{T} \neq 0$. The thrust angle may be found directly from Eq. (22) and the propeller speed is

$$\delta n = \frac{-\tilde{c}u + \sqrt{(\tilde{c}u)^2 + 4\tilde{d}\tilde{T}}}{2\tilde{d}}. \tag{62}$$

Figure 14 illustrates the closed-loop control system, with $\boldsymbol{K}_{\text{ctrl}}$ representing the control law (61). This control law provides the thrust angle δs and, by means of Eq. (62), the propeller speed δn.

Proposition 4.3. *The control law (61) globally asymptotically stabilizes the dynamic system (51)–(55) about the equilibrium* $\boldsymbol{\eta} = \boldsymbol{0}$ *and* $\boldsymbol{\xi} = \boldsymbol{0}$ *and* e_{ψ} *remains bounded and converges asymptotically to zero provided* β_r, χ_r, δs_r, u_r, *and* δn_r *are bounded,* $\tilde{T} \neq 0$, *and* $-\frac{a_{\beta}}{1+b_{\beta}} < 0$.

Proof: The proof of Proposition 4.3 follows from Lyapunov stability analysis of the closed-loop system (Khalil, 2002). For simplicity, we consider only the special case in which the parameters a_{β} and b_{β} do not change values due to model switching; the discontinuities that are introduced by these isolated changes in parameter values can be addressed with slight modifications of the Lyapunov function (Liberzon, 2002). Consider the error dynamics in Eqs. (51)–(55). Choose the radially unbounded candidate Lyapunov function

$$V_2 = \frac{1}{2}\eta_1^2 + \frac{1}{2}\eta_2^2 + \frac{1}{2}\eta_3^2 + \frac{1}{2}[\boldsymbol{\xi} - \boldsymbol{\phi}(\boldsymbol{\eta})]^T[\boldsymbol{\xi} - \boldsymbol{\phi}(\boldsymbol{\eta})] > 0. \tag{63}$$

Applying the control law (61), the time derivative of Eq. (63) is

$$\dot{V}_2 = -\kappa_3\eta_1 \tanh(\kappa_4\eta_1) - \kappa_1\eta_3 \tanh(\kappa_1\eta_3) - [\boldsymbol{\xi} - \boldsymbol{\phi}(\boldsymbol{\eta})]^T \boldsymbol{K}[\boldsymbol{\xi} - \boldsymbol{\phi}(\boldsymbol{\eta})] \leq 0.$$

Using Lemma 4.1 for the $\boldsymbol{\eta}$ subsystem, and recalling that $\boldsymbol{K}$ is positive definite, the equilibrium is globally asymptotically stable by Lyapunov's direct method, provided e_{ψ} is bounded so that the input (61) remains well-defined.

Rearranging the ξ_1 transform in Eq. (50) gives

$$\dot{e}_{\psi} = \frac{a_{\beta}}{b_{\beta} + 1}e_{\psi} + \frac{1}{b_{\beta} + 1}\xi_1. \tag{64}$$

Since $\frac{a_{\beta}}{1+b_{\beta}} < 0$, the system (64) is exponentially stable. Since ξ_1 remains bounded while the input (61) is well-defined, e_{ψ} (and $\dot{e}_{\psi}$) remains bounded; see Lemma 4.6 in Khalil (2002). Futhermore, as ξ_1 converges to zero, so do e_{ψ} and $\dot{e}_{\psi}$. □

At higher speeds, the sideslip dynamics become extremely stable and β remains very close to zero. Rather than vary the structure of the speed-scheduled steering dynamics by eliminating β as a state variable, we set $a_{\beta} = 0$ and $b_{\beta} = 0$ with the understanding that β remains zero in this higher-speed regime. Referring to Eq. (50), we see that $\xi_1 = \dot{e}_{\psi}$, in this case. The dynamics Eq. (56) are then superfluous; the ξ_1 dynamics are given by Eq. (54). In this scenario, the control law (61) globally asymptotically stabilizes [Eqs. (51)–(55)].

To compare the PD control law with the backstepping control law, we linearize the error dynamics (38)–(40), under the feedback control law (61). The resulting state matrix is given in Appendix C.

The state matrix for the linearized tracking error dynamics using the backstepping control approach is given in Appendix C. The structure of the state matrix is similar to that for the PD cascade approach, though there are additional nonzero terms in the backstepping state matrix.

15564967, 2013, 30, Downloaded from https://onlinelibrary.wiley.com. By Universita Di Pavia- on [25/11/2021]. Re-use and distribution is strictly not permitted, except for Open Access articles

Having tuned both controllers heuristically in field trials, the resulting eigenvalues for the linearized backstepping control law are considerably more negative than for the PD control law, suggesting faster convergence and greater robustness. [Explicit values for the control parameters and eigenvalues are given in Sonnenburg and Woolsey (2010).]

Another distinction between the PD control approach and backstepping is that, while the former approach requires six gains to be tuned at *each* nominal speed, the backstepping approach involves nine gains that, once tuned, are valid over the full speed envelope. Adjusting κ_1 and κ_2 varies how aggressively the vessel points toward the desired position. Increasing κ_5 is analogous to increasing the "look ahead" distance in line of sight guidance. Increasing κ_3 and κ_4 increases how aggressively the vessel speeds toward the desired position.

Accommodating Speed-Scheduled Model Parameters. The results in Section 3.3 show that linear speed and steering models, with a speed-scheduled set of model parameters, adequately describe the dynamics of the Ribcraft USV. Earlier formulations of the backstepping control law on which the approach in Section 4.3 is based (Jiang and Nijmeijer, 1997; Jiang et al., 2001) assume that a single set of model parameters is used. The backstepping control law must be modified to include a speed-scheduled set of model parameters. The model parameters used to create the reference trajectory switch values when the reference speed varies significantly. The vessel's actual speed and the reference speed may fall into different regimes, corresponding to different model parameter values. The trajectory tracking control law must account for these disparities.

Let the subscript "r" denote parameter values associated with the reference trajectory at a given instant; parameters without this subscript correspond to the vessel's actual speed. Differentiating Eqs. (34)–(37), we have

$$\dot{e}_u = a_u e_u + \tilde{T}_\mathrm{r} - \tilde{T} + \Delta a_u u_\mathrm{r} + \Delta b_{u_\mathrm{bias}},$$

$$\begin{pmatrix} \dot{e}_\chi \\ \dot{e}_\psi \\ \ddot{e}_\psi \end{pmatrix} = \begin{pmatrix} a_\beta & -a_\beta & 1+b_\beta \\ 0 & 0 & 1 \\ 0 & 0 & a_r \end{pmatrix} \begin{pmatrix} e_\chi \\ e_\psi \\ \dot{e}_\psi \end{pmatrix} + \begin{pmatrix} 0 \\ 0 \\ b_r \end{pmatrix} (\tilde{T}_\mathrm{r}\delta s_\mathrm{r} - \tilde{T}\delta s) + \begin{pmatrix} \Delta a_\beta \chi_\mathrm{r} - \Delta a_\beta \psi_\mathrm{r} + \Delta b_\beta \dot{\psi}_\mathrm{r} + \Delta b_{\beta_\mathrm{bias}} \\ 0 \\ \Delta a_r \dot{\psi}_\mathrm{r} + \Delta b_r \tilde{T}_\mathrm{r}\delta s_\mathrm{r} + \Delta b_{r_\mathrm{bias}} \end{pmatrix},$$

where

$$\begin{aligned} \Delta a_u &= a_{u_\mathrm{r}} - a_u, \\ \Delta b_{u_\mathrm{bias}} &= b_{u_{\mathrm{bias_r}}} - b_{u_\mathrm{bias}}, \\ \Delta b_{\beta_\mathrm{bias}} &= b_{\beta_{\mathrm{bias_r}}} - b_{\beta_\mathrm{bias}}, \\ \Delta a_\beta &= a_{\beta_\mathrm{r}} - a_\beta, \\ \Delta b_\beta &= b_{\beta_\mathrm{r}} - b_\beta, \\ \Delta a_r &= a_{r_\mathrm{r}} - a_r, \\ \Delta b_r &= b_{r_\mathrm{r}} - b_r, \\ \Delta b_{r_\mathrm{bias}} &= b_{r_{\mathrm{bias_r}}} - b_{r_\mathrm{bias}}. \end{aligned}$$

The change of variables

$$\begin{pmatrix} \boldsymbol{\eta} \\ \boldsymbol{\xi} \\ e_\psi \end{pmatrix} = \begin{pmatrix} \eta_1 \\ \eta_2 \\ \eta_3 \\ \xi_1 \\ \xi_2 \\ e_\psi \end{pmatrix} = \begin{pmatrix} e_s \\ e_y \\ e_\chi \\ -a_\beta e_\psi + (b_\beta + 1)\dot{e}_\psi + (\Delta a_\beta \chi_\mathrm{r} - \Delta a_\beta \psi_\mathrm{r} + \Delta b_\beta \dot{\psi}_\mathrm{r} + \Delta b_{\beta_\mathrm{bias}}) \\ e_u \\ e_\psi \end{pmatrix}$$

gives the transformed trajectory tracking error dynamics,

$$\dot{\eta}_1 = (\dot{\chi}_\mathrm{r} - a_\beta \eta_3 + \xi_1)\eta_2 - u_\mathrm{r} + \xi_2 + u_\mathrm{r}\cos\eta_3 \tag{65}$$

$$\dot{\eta}_2 = -(\dot{\chi}_\mathrm{r} - a_\beta \eta_3 + \xi_1)\eta_1 + u_\mathrm{r}\sin\eta_3 \tag{66}$$

$$\dot{\eta}_3 = a_\beta \eta_3 + \xi_1, \tag{67}$$

$$\begin{aligned} \dot{\xi}_1 = {} & \left(\frac{a_r(b_\beta+1) - a_\beta}{1+b_\beta}\right)\xi_1 + \left(\frac{(a_r(b_\beta+1) - a_\beta)a_\beta}{1+b_\beta}\right) e_\psi \\ & + b_r(b_\beta+1)(\tilde{T}_\mathrm{r}\delta s_\mathrm{r} - \tilde{T}\delta s) \\ & + (1+b_\beta)(\Delta a_r \dot{\psi}_\mathrm{r} + b_{r_\mathrm{r}} T_\mathrm{r}\delta s_\mathrm{r} + \Delta b_{r_\mathrm{bias}}) \\ & - \frac{[a_r(1+b_\beta) - a_\beta](\Delta a_\beta \chi_\mathrm{r} - \Delta a_\beta \psi_\mathrm{r} + \Delta b_\beta \dot{\psi}_\mathrm{r} + \Delta b_{\beta_\mathrm{bias}})}{1+b_\beta} \\ & + (\Delta a_\beta \dot{\chi}_r - \Delta a_\beta \dot{\psi}_r + \Delta b_\beta \ddot{\psi}_r), \end{aligned} \tag{68}$$

$$\dot{\xi}_2 = a_u \xi_2 + \tilde{T}_\mathrm{r} - \tilde{T} + \Delta a_u u_\mathrm{r} + \Delta b_{u_\mathrm{bias}}, \tag{69}$$

$$\begin{pmatrix} \dot{e}_\psi \\ \ddot{e}_\psi \end{pmatrix} = \begin{pmatrix} 0 & 1 \\ 0 & a_r \end{pmatrix} \begin{pmatrix} e_\psi \\ \dot{e}_\psi \end{pmatrix} + \begin{pmatrix} 0 \\ b_r \end{pmatrix} (\tilde{T}_\mathrm{r}\delta s_\mathrm{r} - \tilde{T}\delta s) + \begin{pmatrix} 0 \\ \Delta a_r \dot{\psi}_\mathrm{r} + \Delta b_r \tilde{T}_\mathrm{r}\delta s_\mathrm{r} + \Delta b_{r_\mathrm{bias}} \end{pmatrix}. \tag{70}$$

Compare with the original backstepping error dynamics (51)–(56).

Augmenting the original control to accommodate the discrepancy in actual and reference model parameters simply requires adjusting the outer loop steering and speed

15564967, 2013, 30, Downloaded from https://onlinelibrary.wiley.com. By Universita Di Pavia- on [25/11/2021]. Re-use and distribution is strictly not permitted, except for Open Access articles

dynamics as follows:

$$\begin{aligned}
\begin{pmatrix}\tilde{T}\,\delta s\\ \tilde{T}\end{pmatrix} &= \begin{pmatrix}\tilde{T}_{\mathrm{r}}\,\delta s_{\mathrm{r}}\\ \tilde{T}_{\mathrm{r}}\end{pmatrix} + \begin{pmatrix}\frac{1}{b_r(b_\beta+1)} & 0\\ 0 & 1\end{pmatrix} \times \left[\begin{pmatrix}\frac{a_r(b_\beta+1)-a_\beta}{1+b_\beta}\,\xi_1 + \frac{[a_r(b_\beta+1)-a_\beta]a_\beta}{1+b_\beta}\,e_\psi\\ a_u\xi_2\end{pmatrix}\right.\\
&+\begin{pmatrix}(1+b_\beta)(\Delta a_r\dot{\psi}_{\mathrm{r}} + b_{r_{\mathrm{r}}}T_{\mathrm{r}}\delta s_{\mathrm{r}} + \Delta b_{r_{\mathrm{bias}}}) - \frac{[a_r(1+b_\beta)-a_\beta](\Delta a_\beta\chi_{\mathrm{r}} - \Delta a_\beta\psi_{\mathrm{r}} + \Delta b_\beta\dot{\psi}_{\mathrm{r}} + \Delta b_{\beta_{\mathrm{bias}}})}{1+b_\beta}\\ \Delta a_u u_{\mathrm{r}} + \Delta b_{u\,\mathrm{bias}}\end{pmatrix}\\
&+\begin{pmatrix}\Delta a_\beta\dot{\chi}_r - \Delta a_\beta\dot{\psi}_r + \Delta b_\beta\ddot{\psi}_r\\ 0\end{pmatrix} - \begin{pmatrix}\left[-\int_0^1 \cos(s\eta_3)ds\,\kappa_5 u_{\mathrm{r}}\right][-(\dot{\chi}_{\mathrm{r}} - a_\beta\eta_3 + \xi_1)\eta_1 + \kappa_5 u_{\mathrm{r}}\sin\eta_3]\\ -\kappa_3\kappa_4\mathrm{sech}^2(\kappa_4\eta_1)[(\dot{\chi}_{\mathrm{r}} - a_\beta\eta_3 + \xi_1)\eta_2 + \kappa_5(-u_{\mathrm{r}} + u_{\mathrm{r}}\cos\eta_3 + \xi_2)]\end{pmatrix}\\
&-\left(\begin{pmatrix}\left[-\int_0^1 \sin(s\eta_3)sds\,\eta_2\kappa_5 u_{\mathrm{r}} - \kappa_1\kappa_2\mathrm{sech}^2(\kappa_2\eta_3) - a_\beta\right](a_\beta\eta_3 + \xi_1)\\ u_{\mathrm{r}}\sin\eta_3(a_\beta\eta_3 + \xi_1)\end{pmatrix} + \begin{pmatrix}\eta_3\\ \eta_1\end{pmatrix}\right.\\
&\left.\left.+\boldsymbol{K}\begin{pmatrix}\xi_1 + \left[\int_0^1 \cos(s\eta_3)ds\right]\eta_2\kappa_5 u_{\mathrm{r}} + \kappa_1\tanh(\kappa_2\eta_3) + a_\beta\eta_3\\ \xi_2 - u_{\mathrm{r}} + u_{\mathrm{r}}\cos\eta_3 + \kappa_3\tanh(\kappa_4\eta_1)\end{pmatrix}\right]. \qquad (71)
\end{aligned}$$

This modified control law cancels the additional terms. Closed-loop stability properties follow as for Eq. (61).

Proposition 4.4. *The control law (71) globally asymptotically stabilizes the dynamic system (65)–(69) about the equilibrium* $(\boldsymbol{\eta}, \boldsymbol{\xi}) = (\mathbf{0}, \mathbf{0})$ *and* e_ψ *remains bounded and converges to zero, provided* β_{r}, χ_{r}, δs_{r}, u_{r}, *and* δn_{r} *are bounded and* $\tilde{T} \neq 0$.

The proof Proposition 4.4 follows similarly the proof of Proposition 4.3.

4.4. Trajectory Tracking Results

Due to the hierarchal nature of the PD trajectory controller, lower-level controllers are tested first. Incrementally higher-level controllers are tested until finally the trajectory controllers are tested. The performance of the thrust angle and propeller speed control are first tested. The trajectory control algorithms defined in Sections 4.2 and 4.3 assume thrust angle and propeller speed are directly controlled. In reality, a motor controller actuates hydraulics that drive the gimbal assembly and a throttle actuator sets the throttle position. A PID loop implemented on the motor controller controls thrust angular motion. A PID controller, coupled with a nonlinear steady-state gain mapping, controls propeller speed. Figures 15(a) and (b) show thrust angle and propeller speed performance, respectively.

Heading control is tested for forward motion, with PD parameters tuned to accommodate rate limiting in the actuators. Figure 16(a) shows the boat tracking to a northern heading after facing south. The ratio between proportional and derivative gain varies for different traces, illustrating the effects of derivative control on a system with rate-limited inputs. Too much derivative gain causes the system to oscillate on its way to a zero heading, while too little derivative gain causes the system to overshoot considerably. The ideal ratio between proportional and derivative control yields no oscillatory behavior or overshoot. This ratio is a function of the rate limit and the maximum achievable turn rate. The rate limit stays constant through the operating envelope, but the maximum turn rate varies, requiring use of gain scheduling with speed.

Wrapping the speed controller around the propeller speed control results in good speed tracking. Figure 16(b) shows the boat tracking desired speed by sending propeller speed commands to the propeller speed controller. The speed tracking ability demonstrated in Figure 16(b) requires a feedforward propeller speed command that corresponds to the desired forward speed. This feedforward propeller speed command is replaced by the open-loop time history of commanded propeller speed when the forward speed controller is incorporated into the PD cascade described in Section 4.2.

Figure 17 illustrates controller performance for a reference trajectory that has constant propeller speed and a sinusoidally varying thrust angle. (All trajectories begin at the origin.) Circles and vectors denote position and velocity at 10 s intervals. The backstepping control law results in fast convergence to the reference trajectory, with the actual path staying within just a few meters of the desired path. The PD cascade control law results in slightly poorer tracking performance.

Figure 18 shows the performance of the trajectory controllers with a reference trajectory that has a sinusoid in propeller speed coupled with a sinusoid (of higher frequency) in thrust angle. (Again, all trajectories begin at the origin.) As in Figure 17, circles and velocity vectors denote position and velocity at 10 s intervals. This reference trajectory contains aggressive maneuvering, including taking sharp turns during hard deceleration and acceleration. Since the reference speed varies, parameter switching in the control

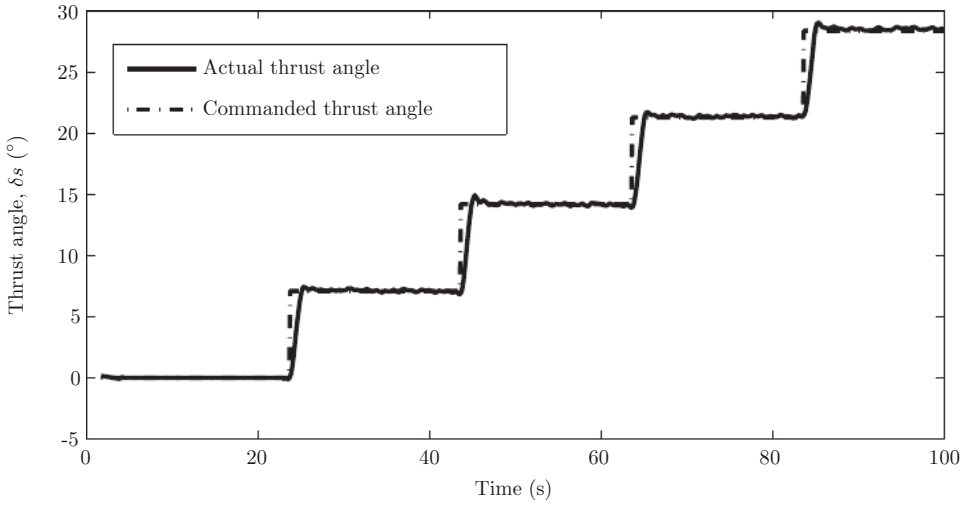

(a) The Ribcraft USV tracking to commanded thrust angle

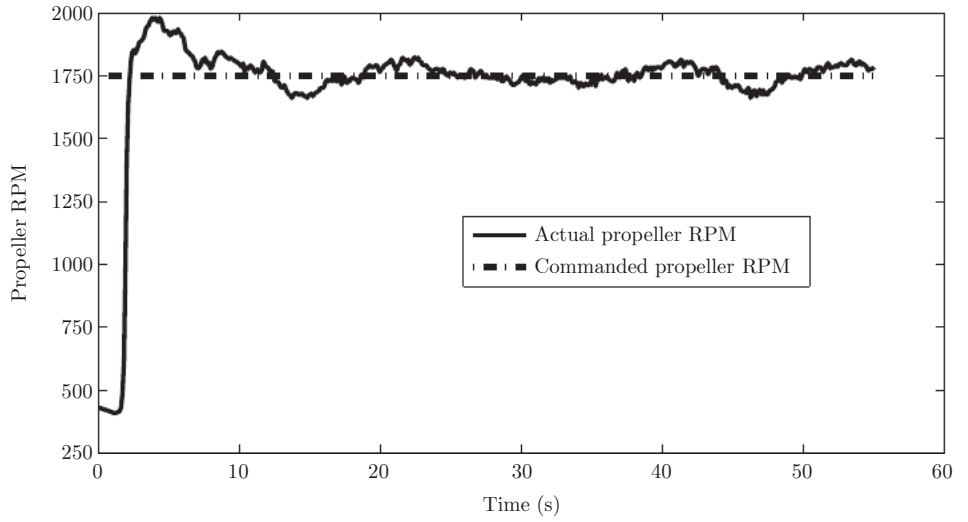

(b) The Ribcraft USV tracking to commanded propeller speed

Figure 15. Actuator control performance.

laws is tested. Furthermore, such an aggressive reference trajectory tests the controllers' effectiveness in the presence of unmodeled dynamics, including interaction with wake dynamics that are noticeable during simultaneous deceleration and turning. The backstepping trajectory control law forces convergence to the reference trajectory, and the vessel stays within a few meters of the desired position, though oscillations are noticeable when wake dynamics become prevalent. The PD cascade control law results in qualitatively correct behavior, but the vessel's trajectory fails to converge to the reference trajectory.

The backstepping control law clearly outperforms the PD cascade control law for the field tests presented in Figures 17 and 18. For steady speed reference trajectories, the PD cascade control law oscillates about the reference trajectory while the backstepping control law converges quickly. For variable speed reference trajectories, the PD cascade control law's performance degrades considerably while the backstepping control law converges to the reference trajectory.

5. CONCLUSIONS

A set of linear dynamic models with experimentally identified parameters were compared for a planing USV with an outboard motor. The results indicate that thrust is well modeled by a simple bilinear thruster model. Experiments also indicate that the USV experiences significant sideslip when

15564967, 2013, 30, Downloaded from https://onlinelibrary.wiley.com. By Universita Di Pavia- on [25/11/2021]. Re-use and distribution is strictly not permitted, except for Open Access articles

15564967, 2013, 30, Downloaded from https://onlinelibrary.wiley.com. By Universita Di Pavia- on [25/11/2021]. Re-use and distribution is strictly not permitted, except for Open Access articles

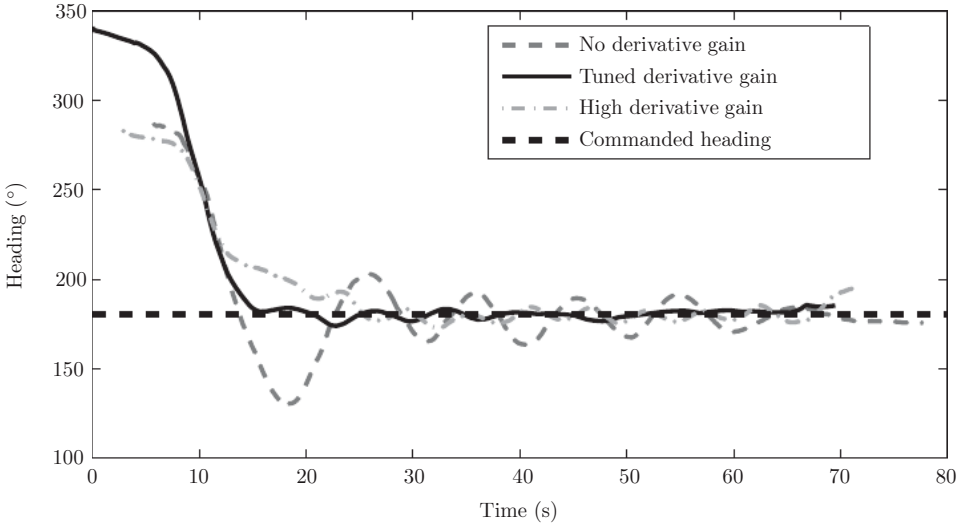

(a) The Ribcraft USV tracking to commanded heading for different ratios of proportional and derivative gains

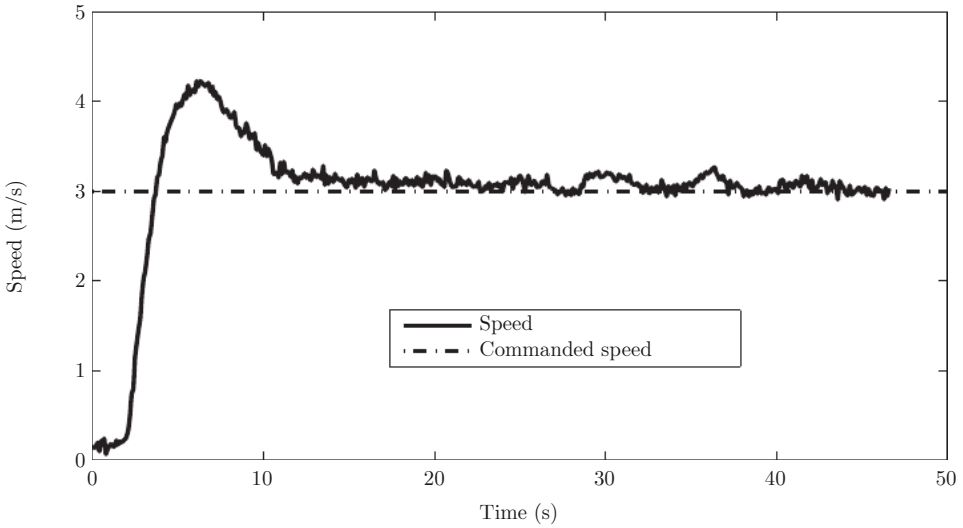

(b) The Ribcraft USV tracking to commanded speed

Figure 16. Heading and speed tracking performance.

operating at low speed, though at higher speeds sideslip becomes less prevalent. Parameters for the speed and steering models are scheduled based on a discrete set of nominal speeds. For low-speed motion, the steering dynamics are well-approximated using first-order lag models for turn rate and sideslip, a four-parameter steering model that can be easily identified from available motion data. At higher speeds, the steering motion is well-modeled by a first-order lag model for turn rate, containing only two parameters. A first-order linear speed model accurately captures the speed dynamics. These models, with speed-scheduled parameters, can be used to generate dynamically feasible trajectories for the USV to track.

Theoretical and experimental performance results for two trajectory tracking controllers were also presented and compared. The first approach to trajectory tracking control involves a cascade of proportional-derivative compensators, which was shown to be locally exponentially stabilizing for a class of simple trajectories. In field experiments, the approach worked reasonably well for benign trajectories (e.g., constant-speed trajectories with gradual turns). For more aggressive, variable speed trajectories, the PD cascade approach performs quite poorly. A nonlinear backstepping control law was also developed and was shown to result in global asymptotic convergence of the tracking error variables of interest. In field trials, the backstepping

15564967, 2013, 30, Downloaded from https://onlinelibrary.wiley.com. By Universita Di Pavia- on [25/11/2021]. Re-use and distribution is strictly not permitted, except for Open Access articles

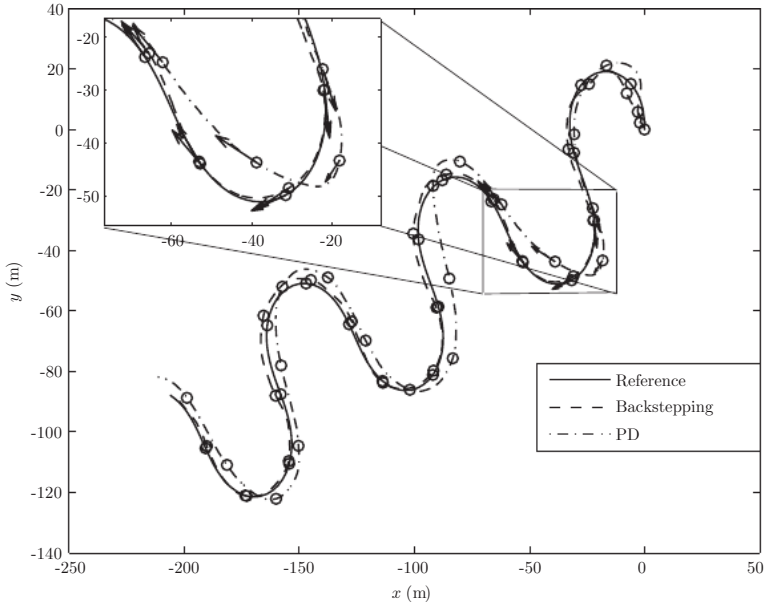

Figure 17. Trajectory control for constant propeller speed and a sinusoid in thrust angle.

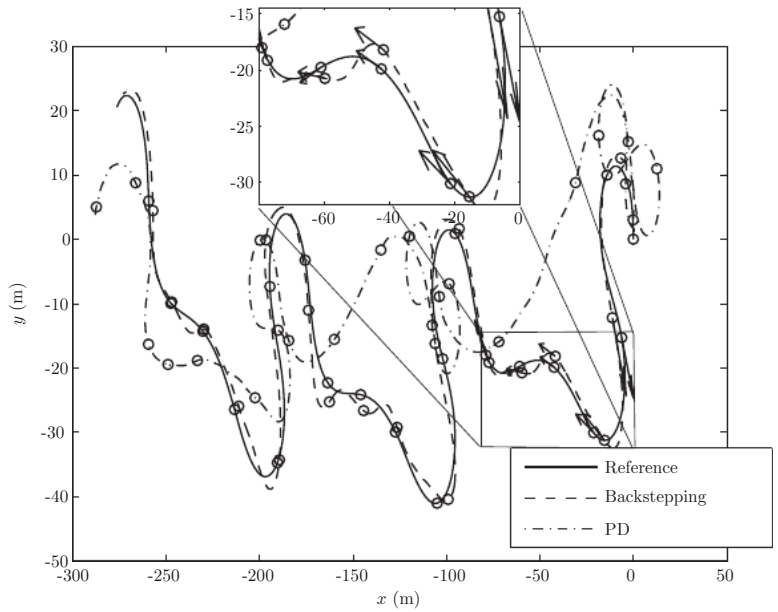

Figure 18. Trajectory control for sinusoids (of differing frequency) in propeller speed and thrust angle.

approach resulted in excellent tracking performance, even for aggressive, variable speed trajectories.

Ongoing work is focused on expanding the theoretical results to accommodate switching between forward and reverse motion. In practice, it is expected that scenarios would arise in which a riverine USV must stop and then move backward, in order to extricate itself from an unnavigable waterway. Factors that complicate theoretical analysis include a mathematical singularity at zero speed and, more importantly, the nonlinear (bistable) dynamics of reverse motion.

ACKNOWLEDGMENTS

The authors gratefully acknowledge the critical comments of the anonymous reviewers and the support of the U.S.

Office of Naval Research under Grants No. N00014-10-1-0185 and N00014-11-1-0532.

APPENDIX A: EXPRESSIONS f_ψ AND f_u IN EQS. (48) AND (49)

The f_ψ and f_n expressions shown in the closed loop PD cascade error dynamics are

$$
\begin{aligned}
f_\psi(e_s, e_y, e_\chi, e_\psi, e_{\dot\psi}, e_u) &= \delta s_r\left(\tilde c\delta n_r u_r + \tilde d\delta n_r^2\right)\\
&- [k_{d_\psi}(k_{p_y}\{k_{e_s}[a_\beta e_\chi - a_\beta e_\psi + (b_\beta+1)e_r - \dot\chi_r]\\
&+ u_r\sin(e_\chi)\} + e_r) + \delta s_r + p_\psi(e_\psi + e_y k_{p_y})]\\
&\times\left(\frac{1}{2\tilde d k_{d_u}^2}\tilde c(u_r - e_u)\left[2a_\beta\tilde d k_{d_u}^2 e_\chi e_y k_{p_s} - 2a_\beta\tilde d k_{d_u}^2 e_\psi e_y k_{p_s}\right.\right.\\
&+\left(-4a_\beta\tilde d k_{d_u}^2 e_\chi e_y k_{p_s} + 4a_\beta\tilde d k_{d_v}^2 e_\psi e_y k_{p_s} + 4a_u\tilde d k_{d_v}^2 e_u\right.\\
&- 4b_\beta\tilde d k_{d_u}^2 e_r e_y k_{p_s} + \tilde c^2 k_{d_u}^2 e_u^2 - 2\tilde c^2 k_{d_u}^2 e_u u_r + \tilde c^2 k_{d_u}^2 u_r^2\\
&+ 4\tilde c\tilde d\delta n_r k_{d_u}^2 u_r - 2\tilde c k_{d_u} e_u + 2\tilde c k_{d_v} u_r + 4\tilde d^2\delta n_r^2 k_{d_u}^2\\
&+ 4\tilde d\dot\chi_r k_{d_u}^2 e_y k_{p_s} - 4\tilde d k_{d_u}^2 e_r e_y k_{p_s} + 4\tilde d k_{d_u}^2 e_u k_{p_s}\\
&+ 4\tilde d k_{d_u}^2 k_{p_s} u_r\cos(e_\chi) - 4\tilde d k_{d_v}^2 k_{p_s} u_r + 4\tilde d\delta n_r k_{d_u}\\
&+ 4\tilde d k_{d_u} e_s k_{p_s} k_{p_u} + 4\tilde d k_{d_u} e_u k_{p_u} + 1\big)^{\frac{1}{2}} + 2b_\beta\tilde d k_{d_u}^2 e_r e_y k_{p_s}\\
&+ \tilde c k_{d_u} e_u - \tilde c k_{d_u} u_r - 2\tilde d\dot\chi_r k_{d_u}^2 e_y k_{p_s} + 2\tilde d k_{d_u}^2 e_r e_y k_{p_s}\\
&- 2\tilde d k_{d_u}^2 e_u k_{p_s} - 2\tilde d k_{d_u}^2 k_{p_s} u_r\cos(e_\chi) + 2\tilde d k_{d_u}^2 k_{p_s} u_r\\
&\left.\left.- 2\tilde d\delta n_r k_{d_u} - 2\tilde d k_{d_u} e_s k_{p_s} k_{p_u} - 2\tilde d k_{d_u} e_u k_{p_u} - 1\right]\right.\\
&+\frac{1}{4\tilde d k_{d_u}^4}\left[2a_\beta\tilde d k_{d_u}^2 e_\chi e_y k_{p_s} - 2a_\beta\tilde d k_{d_u}^2 e_\psi e_y k_{p_s}\right.\\
&+\left(-4a_\beta\tilde d k_{d_u}^2 e_\chi e_y k_{p_s} + 4a_\beta\tilde d k_{d_u}^2 e_\psi e_y k_{p_s} + 4a_u\tilde d k_{d_u}^2 e_u\right.\\
&- 4b_\beta\tilde d k_{d_u}^2 e_r e_y k_{p_s} + \tilde c^2 k_{d_u}^2 e_u^2 - 2\tilde c^2 k_{d_u}^2 e_u u_r + \tilde c^2 k_{d_u}^2 u_r^2\\
&+ 4\tilde c\tilde d\delta n_r k_{d_u}^2 u_r - 2\tilde c k_{d_u} e_u + 2\tilde c k_{d_u} u_r + 4\tilde d^2\delta n_r^2 k_{d_u}^2\\
&+ 4\tilde d\dot\chi_r k_{d_u}^2 e_y k_{p_s} - 4\tilde d k_{d_u}^2 e_r e_y k_{p_s} + 4\tilde d k_{d_u}^2 e_u k_{p_s}\\
&+ 4\tilde d k_{d_u}^2 k_{p_s} u_r\cos(e_\chi) - 4\tilde d k_{d_u}^2 k_{p_s} u_r + 4\tilde d\delta n_r k_{d_u}\\
&+ 4\tilde d k_{d_u} e_s k_{p_s} k_{p_u} + 4\tilde d k_{d_u} e_u k_{p_u} + 1\big)^{\frac{1}{2}} + 2b_\beta\tilde d k_{d_u}^2 e_r e_y k_{p_s}\\
&+ \tilde c k_{d_u} e_u - \tilde c k_{d_u} u_r - 2\tilde d\dot\chi_r k_{d_u}^2 e_y k_{p_s} + 2\tilde d k_{d_u}^2 e_r e_y k_{p_s}\\
&- 2\tilde d k_{d_u}^2 e_u k_{p_s} - 2\tilde d k_{d_u}^2 k_{p_s} u_r\cos(e_\chi) + 2\tilde d k_{d_u}^2 k_{p_s} u_r\\
&\left.\left.- 2\tilde d\delta n_r k_{d_u} - 2\tilde d k_{d_u} e_s k_{p_s} k_{p_u} - 2\tilde d k_{d_u} e_u k_{p_u} - 1\right]^2\right) \qquad \text{(A.1)}
\end{aligned}
$$

and

$$
\begin{aligned}
f_u(e_s, e_y, e_\chi, e_\psi, e_{\dot\psi}, e_u) &= \frac{1}{2\tilde d k_{d_u}^2}\left[2a_\beta\tilde d k_{d_u}^2 e_\chi e_y k_{p_s}\right.\\
&- 2a_\beta\tilde d k_{d_u}^2 e_\psi e_y k_{p_s} + \left(-4a_\beta\tilde d k_{d_u}^2 e_\chi e_y k_{p_s} + 4a_\beta\tilde d k_{d_u}^2 e_\psi e_y k_{p_s}\right.\\
&\left.\left.+ 4a_u\tilde d k_{d_u}^2 e_u - 4b_\beta\tilde d k_{d_u}^2 e_r e_y k_{p_s} + \tilde c^2 k_{d_u}^2 (e_u - u_r)^2\right.\right.\\
&+ 2\tilde c k_{d_u}(2\tilde d\delta n_r k_{d_u} u_r - e_u + u_r) + 4\tilde d^2\delta n_r^2 k_{d_u}^2 + 4\tilde d\dot\chi_r k_{d_u}^2 e_y k_{p_s}\\
&- 4\tilde d k_{d_u}^2 e_r e_y k_{p_s} + 4\tilde d k_{d_u}^2 e_u k_{p_s} + 4\tilde d k {d_u}^2 k_{p_s} u_r\cos(e_\chi)\\
&- 4\tilde d k_{d_u}^2 k_{p_s} u_r + 4\tilde d\delta n_r k_{d_u} + 4\tilde d k_{d_u} e_s k_{p_s} k_{p_u}\\
&\left.\left.+ 4\tilde d k_{d_u} e_u k_{p_u} + 1\big)^{\frac{1}{2}} + 2b_\beta\tilde d k_{d_u}^2 e_r e_y k_{p_s} + \tilde c k_{d_u} e_u - \tilde c k_{d_u} u_r\right.\right.\\
&- 2\tilde d\dot\chi_r k_{d_u}^2 e_y k_{p_s} + 2\tilde d k_{d_u}^2 e_r e_y k_{p_s} - 2\tilde d k_{d_u}^2 e_u k_{p_s}\\
&- 2\tilde d k_{d_u}^2 k_{p_s} u_r\cos(e_\chi) + 2\tilde d k_{d_u}^2 k_{p_s} u_r - 2\tilde d\delta n_r k_{d_u}\\
&\left.- 2\tilde d k_{d_u} e_s k_{p_s} k_{p_u} - 2\tilde d k_{d_u} e_u k_{p_u} - 1\right]. \qquad \text{(A.2)}
\end{aligned}
$$

APPENDIX B: LINEARIZED TRACKING ERROR DYNAMICS FOR THE CASCADED PD CONTROL APPROACH

The state matrix for the linearized dynamics is

$$
\begin{pmatrix}\dot e_s\\ \dot e_y\\ \dot e_\chi\\ \dot e_\psi\\ \ddot e_\psi\\ \dot e_u\end{pmatrix} = \begin{pmatrix}0 & \dot\chi_r & 0 & 0 & 0 & 1\\ -\dot\chi_r & 0 & u_r & 0 & 0 & 0\\ 0 & 0 & -a_\beta & b_\beta+1 & 0 & 0\\ 0 & 0 & a_\beta & 0 & 1 & 0\\ a_{51} & a_{52} & a_{53} & a_{54} & a_{55} & a_{56}\\ a_{61} & a_{62} & 0 & 0 & 0 & a_{66}\end{pmatrix}\begin{pmatrix}e_s\\ e_y\\ e_\chi\\ e_\psi\\ \dot e_\psi\\ e_u\end{pmatrix} \qquad \text{(B.1)}
$$

where

$$
\begin{aligned}
a_{51} &= b_r\left\{\dot\chi_r k_{d_\psi} k_{p_y}\left(\tilde c u_r\varphi_2 + \varphi_2^2\right) - \frac{\delta s_r}{k_{d_v}}\left[\tilde c u_r k_{p_s} k_{p_u}\left(\frac{1}{\varphi_1} - 1\right)\right.\right.\\
&\left.\left.+\varphi_2\left(\frac{2\tilde d k_{p_s} k_{p_u}}{\varphi_1} - 2\tilde d k_{p_s} k_{p_u}\right)\right]\right\},\\
a_{52} &= b_r\left\{-k_{p_\psi} k_{p_y}\left(\tilde c u_r\varphi_3 + \varphi_3^2\right) + \delta s_r\left[\tilde c u_r\dot\chi_r k_{p_s}\left(\frac{1}{\varphi_1} + 1\right)\right.\right.\\
&\left.\left.+\varphi_3\left(\frac{2\tilde d\dot\chi_r k_{p_s}}{\varphi_1} + 2\tilde d\dot\chi_r k_{p_s}\right)\right]\right\},\\
a_{53} &= -b_r k_{d_\psi} k_{p_y} u_r\left(\tilde c u_r\varphi_3 + \varphi_3^2\right),\\
a_{54} &= -b_r k_{p_\psi}\left(\tilde c u_r\varphi_3 + \varphi_3^2\right),\\
a_{55} &= a_r - b_r k_{d_\psi}\left(\tilde c u_r\varphi_3 + \varphi_3^2\right),\\
a_{56} &= -b_r\delta s_r\left[\left(-\frac{\varphi_4}{2\varphi_1} + \tilde c k_{d_u} - 2\tilde d k_{d_u}^2 k_{p_s} - 2\tilde d k_{d_u} k_{p_u}\right)\right.\\
&\left.\times\left(\frac{\tilde c u_r}{2\tilde d k_{d_u}^2} + 1\right) + \frac{\varphi_3}{k_{d_u}^2} - \tilde c\varphi_3\right],\\
a_{61} &= -\frac{k_{p_s} k_{p_u}}{k_{d_u}}\left(\frac{1}{\varphi_1} + 1\right),\\
a_{62} &= -\dot\chi_r k_{p_s}\left(\frac{1}{\varphi_1} + 1\right),\\
a_{66} &= \frac{1}{2\tilde d k_{d_u}^2}\left(-\frac{\varphi_4}{2\varphi_1} + \tilde c k_{d_u} - 2\tilde d k_{d_u}^2 k_{p_s} - 2\tilde d k_{d_u} k_{p_u}\right),
\end{aligned}
$$

15564967, 2013, 30, Downloaded from https://onlinelibrary.wiley.com. By Universita Di Pavia- on [25/11/2021]. Re-use and distribution is strictly not permitted, except for Open Access articles

15564967, 2013, 30, Downloaded from https://onlinelibrary.wiley.com. By Universita Di Pavia- on [25/11/2021]. Re-use and distribution is strictly not permitted, except for Open Access articles

with

$$\varphi_1 = \sqrt{\tilde{c}^2 k_{d_u}^2 u_{\mathrm{r}}^2 + 4\tilde{c}\tilde{d}\delta n_{\mathrm{r}} k_{d_u}^2 u_{\mathrm{r}} + 2\tilde{c}k_{d_u} u_{\mathrm{r}} + 4\tilde{d}^2 \delta n_{\mathrm{r}}^2 k_{d_u}^2 + 4\tilde{d}\delta n_{\mathrm{r}} k_{d_u} + 1},$$

$$\varphi_2 = \frac{\sqrt{\tilde{c}^2 k_{d_u}^2 u_{\mathrm{r}}^2 + 4\tilde{c}\tilde{d}\delta n_{\mathrm{r}} k_{d_u}^2 u_{\mathrm{r}} + 2\tilde{c}k_{d_u} u_{\mathrm{r}} + 4\tilde{d}^2 \delta n_{\mathrm{r}}^2 k_{d_u}^2 + 4\tilde{d}\delta n_{\mathrm{r}} k_{d_u} + 1} - \tilde{c}k_{d_u} u_{\mathrm{r}} - 2\tilde{d}\delta n_{\mathrm{r}} k_{d_u} - 1}{2\tilde{d}k_{d_u}^2},$$

$$\varphi_3 = \frac{-\sqrt{\tilde{c}^2 k_{d_u}^2 u_{\mathrm{r}}^2 + 4\tilde{c}\tilde{d}\delta n_{\mathrm{r}} k_{d_u}^2 u_{\mathrm{r}} + 2\tilde{c}k_{d_u} u_{\mathrm{r}} + 4\tilde{d}^2 \delta n_{\mathrm{r}}^2 k_{d_u}^2 + 4\tilde{d}\delta n_{\mathrm{r}} k_{d_u} + 1} - \tilde{c}k_{d_u} u_{\mathrm{r}} - 2\tilde{d}\delta n_{\mathrm{r}} k_{d_u} - 1}{2\tilde{d}k_{d_u}^2},$$

$$\varphi_4 = 4a_u \tilde{d}k_{d_u}^2 - 2\tilde{c}^2 k_{d_u}^2 u_{\mathrm{r}} - 2\tilde{c}k_{d_u} + 4\tilde{d}k_{d_u}^2 k_{p_s} + 4\tilde{d}k_{d_u} k_{p_u}.$$

APPENDIX C: LINEARIZED TRACKING ERROR DYNAMICS FOR THE BACKSTEPPING CONTROL APPROACH

The state matrix for the linearized dynamics is

$$\begin{pmatrix} \dot{e}_s \\ \dot{e}_y \\ \dot{e}_\chi \\ \dot{e}_\psi \\ \ddot{e}_\psi \\ \dot{e}_u \end{pmatrix} = \begin{pmatrix} 0 & \dot{\chi}_{\mathrm{r}} & 0 & 0 & 0 & \kappa_5 \\ -\dot{\chi}_{\mathrm{r}} & 0 & u_r\kappa_5 & 0 & 0 & 0 \\ 0 & 0 & a_\beta & -a_\beta & b_\beta + 1 & 0 \\ 0 & 0 & 0 & 0 & 1 & 0 \\ a_{51} & -\frac{k_1 u_r \kappa 5}{b_\beta + 1} & a_{53} & a_{54} & a_{55} & -\frac{k_2}{b_\beta + 1} \\ a_{61} & a_{62} & a_{63} & a_\beta k_2 & (-b_\beta - 1)k_2 & -k_3 - \kappa_3\kappa_4 \end{pmatrix} \times \begin{pmatrix} e_s \\ e_y \\ e_\chi \\ e_\psi \\ \dot{e}_\psi \\ e_u \end{pmatrix},$$

where

$$a_{51} = \frac{(a_\beta + \dot{\chi}_{\mathrm{r}})u_r\kappa_5 - k_2\kappa_3\kappa_4}{b_\beta + 1},$$

$$a_{53} = -\frac{a_\beta^2 + k_1 a_\beta + \kappa_1\kappa_2 a_\beta + u_r^2\kappa_5^2 + k_1\kappa_1\kappa_2 + 1}{b_\beta + 1},$$

$$a_{54} = \frac{a_\beta(a_\beta + k_1 + \kappa_1\kappa_2)}{b_\beta + 1},$$

$$a_{55} = -\frac{a_\beta b_\beta + (b_\beta + 1)(k_1 + \kappa_1\kappa_2)}{b_\beta + 1},$$

$$a_{61} = -k_3\kappa_3\kappa_4 - 1,$$

$$a_{62} = -\dot{\chi}_{\mathrm{r}}\kappa_3\kappa_4 - k_2 u_r\kappa_5,$$

$$a_{63} = -k_2(a_\beta + \kappa_1\kappa_2).$$

The system is linear and time-invariant provided u_r, δn_r, and $\dot{\chi}_{\mathrm{r}}$ remain constant.

REFERENCES

Abkowitz, M. A. (1964). Lectures on ship hydrodynamics - steering and maneuverability. Technical report, Hydro- and Aerodynamic's Laboratory, Lyngby, Denmark.

Amerongen, J. V. & Cappelle, J. C. V. (1981). Mathematical modelling for rudder roll stabilization. In 6th International Ship Control Systems Symposium, Ottawa, Canada.

Ashrafiuon, H., Muske, K., McNinch, L., & Soltan, R. (2008). Sliding-mode tracking control of surface vessels. IEEE Transactions on Industrial Electronics, 55(11), 4004–4012.

Åström, K. J., & Källström, C. G. (1976). Identification of ship steering dynamics. Automatica, 12, 9–22.

Bertram, V. (2008). Unmanned surface vehicles—A survey. Skibsteknisk Selskab, Copenhagen, Denmark.

Blanke, M. (1981). Ship propulsion losses related to automated steering and prime mover control. Ph.D. thesis, The Technical University of Denmark, Lyngby, Denmark.

Breivik, M., Hovstein, V. E., & Fossen, T. I. (2008). Straight-line target tracking for unmanned surface vehicles. Modeling, Identification, and Control, 29(4), 131–149.

Christensen, A., & Blanke, M. (1986). A linearized state-space model in steering and roll of a high-speed container ship. Technical Report 86-D-574, Servolaboratoriet, Technical University of Denmark, Denmark.

Do, K., Jiang, Z., & Pan, J. (2002a). Underactuated ship global tracking under relaxed conditions. IEEE Transactions on Automatic Control, 47(9), 1529–1536.

Do, K. D., Jiang, Z. P., & Pan, J. (2002b). Universal controllers for stabilization and tracking of underactuated ships. Systems and Control Letters, 47, 299–317.

Faltinsen, O. M. (2005). Hydrodynamics of high-speed marine vehicles. Cambridge University Press.

Fossen, T. I. (1991). Nonlinear modelling and control of underwater vehicles. Ph.D. thesis, The Norwegian Institute of Technology, Trondheim, Norway.

Fossen, T. I. (1995). Guidance and control of ocean vehicles. John Wiley and Sons.

Gadre, A. S., Du, S., & Stilwell, D. J. (2012a). A topological map based approach to long range operation of an unmanned surface vehicle. In American Control Conference (ACC), 2012.

Gadre, A. S., Kragelund, S., Masek, T., Stilwell, D., Woolsey, C., & Horner, D. (2009). Subsurface and surface sensing for autonomous navigation in a riverine environment. In Proceedings to AUVSI's Unmanned Systems, Washington, D.C.

15564967, 2013, 30, Downloaded from https://onlinelibrary.wiley.com. By Universita Di Pavia- on [25/11/2021]. Re-use and distribution is strictly not permitted, except for Open Access articles

Gadre, A. S., Sonnenburg, C., Du, S., Stilwell, D. J., & Woolsey, C. A. (2012b). Guidance and control of an unmanned surface vehicle exhibiting sternward motion. In OCEANS 2012, Hampton, VA.

Godhavn, J.-M. (1996). Nonlinear tracking of underactuated surface vessels. In Proceedings of the 35th Conference on Decision and Control (pp. 975–980), Kobe, Japan.

Grewal, M. S., & Glover, K. (1976). Identifiability of linear and nonlinear dynamical systems. IEEE Transactions on Automatic Control, 21(6), 833–837.

Jategaonkar, R. V. (2006). Flight vehicle system identification: A time domain methodology. American Institute of Aeronautics and Astronautics, Inc.

Jiang, Z.-P. (2002). Global tracking control of underactuated ships by Lyapunov's direct method. Automatica, 38, 301–309.

Jiang, Z.-P., Lefeber, E., & Nijmeijer, H. (2001). Saturated stabilization and tracking of a nonholonomic mobile robot. Systems and Control Letters, 42(5), 327–332.

Jiang, Z.-P., & Nijmeijer, H. (1997). Tracking control of mobile robots: A case study in backstepping. Automatica, 33(7), 1393–1399.

Juang, J.-N. (1994). Applied system identification. Upper Saddle River, NJ: Prentice Hall.

Källström, C. G., & Åström, K. J. (1981). Experience of system identification applied to ship steering. Automatica, 17(1), 187–198.

Khalil, H. (2002). Nonlinear systems. Prentice Hall.

Lefeber, E., Pettersen, K., & Nijmeijer, H. (2003). Tracking control of an underactuated ship. IEEE Transactions on Control Systems Technology, 11(1), 52–61.

Lewandowski, E. M. (2004). The dynamics of marine craft: Maneuvering and seakeeping. Singapore: World Scientific.

Liberzon, D. (2002). Switching in systems and control. Birkhäuser.

Ljung, L. (1999). System identification: Theory for the user, 2nd ed. Prentice Hall.

Manley, J. (2008). New tools for ocean exploration, equipping the NOAA ship Okeanos explorer. In OCEANS 2008, Quebec City, Quebec, Canada.

Morelli, E. A., & Klein, V. (2006). Aircraft system identification: Theory and practice. AIAA.

Muske, K. R., Ashrafinon, H., Haas, G., McCloskey, R., & Flynn, T. (2008). Identification of a control oriented nonlinear dynamic USV model. In American Control Conference, Seattle, WA.

Nguyen, H. D. (2008). Recursive identification of ship manoeuvering dynamics and hydrodynamics. In Mercer, G. N., & Roberts, A. J. (Eds.), Proceedings of the 8th Biennial Engineering Mathematics and Applications Conference, EMAC-2007, Vol. 49 of ANZIAM J. (pp. 717–732).

Nomoto, K., Taguchi, T., Honda, K., & Hirano, S. (1957). On the steering qualities of ships. Technical report, International Shipbuilding Progress, Vol. 4.

Norrbin, N. H. (1970). Theory and observation on the use of a mathematical model for ship maneuvering in deep and confined waters. In 8th Symposium on Naval Hydrodynamics, Pasadena, CA.

Ødegård, V. (2009). Nonlinear identification of ship autopilot models. Master's thesis, Norwegian University of Science and Technology.

Petrich, J. (2009). Improved guidance, navigation, & control for autonomous underwater vehicles: Theory and experiment. Ph.D. thesis, Virginia Polytechnic Institute and State University, Blacksburg, VA.

Petrich, J., & Stilwell, D. J. (2011). Robust control for an autonomous underwater vehicle that suppresses pitch and yaw coupling. Ocean Engineering, 38, 197–204.

Pettersen, K., & Egeland, O. (1997). Robust control of an underactuated surface vessel with thruster dynamics. In Proceedings of the 1997 American Control Conference (Vol. 5, pp. 3411–3415).

Pettersen, K., & Nijmeijer, H. (2000). Semi-global practical stabilization and disturbance adaptation for an underactuated ship. In Proceedings of the 39th IEEE Conference on Decision and Control (Vol. 3, pp. 2144–2149).

Petterson, K. Y., & Egeland, O. (1996). Exponential stabilization of an underactuated surface vessel. In Proceedings of the 35th Conference on Decision and Control (pp. 967–972), Kobe, Japan.

Petterson, K. Y., & Nijmeijer, H. (2001). Underactuated ship tracking control; theory and experiments. International Journal of Control, 74(14), 1435–1446.

Rajesh, G., & Bhattacharyya, S. (2008). System identification for nonlinear maneuvering of large tankers using artificial neural network. Applied Ocean Research, 30(4), 256–263.

Savitzky, A., & Golay, M. J. E. (1964). Smoothing and differentiation of data by simplified least squares procedures. Analytical Chemistry, 36(8), 1627–1639.

Selvam, R. P., Bhattacharyya, S. K., & Haddara, M. (2005). A frequency domain system identification method for linear ship maneuvering. International Shipbuilding Progress, 52(1), 5–27.

Son, K. H., & Nomoto, K. (1981). On the coupled motion of steering and rolling of a high-speed container ship. Journal of the Society of Naval Architecture, 150, 232–244.

Sonnenburg, C., Gadre, A., Horner, D., Kragelund, S., Stilwell, D. J., & Woolsey, C. A. (2010). Control-oriented planar motion modeling of unmanned surface vehicles. In OCEANS 2010, Seattle, WA.

Sonnenburg, C., & Woolsey, C. A. (2010). Control-oriented planar motion modeling of unmanned surface vehicles. Technical Report VaCAS-2011-01, Virginia Center for Autonomous Systems, Blacksburg, VA.

Sri-Jayantha, M., & Stengel, R. F. (1988). Determination of nonlinear aerodynamic coefficients using the estimation-before-modeling method. Journal of Aircraft, 25(9), 796–804.

Stalford, H. L. (1981). High-alpha aerodynamic model identification of t-2c aircraft using the ebm method. Journal of Aircraft, 18(10), 801–809.

Stengel, R. F. (1986). Optimal control and estimation. Mineola, NY: Dover Publications.

Stilwell, D. J., Gadre, A. S., & Kurdila, A. J. (2011). A receding horizon approach to generating dynamically feasible plans for vehicles that operate over large areas. In Intelligent Robots and Systems (IROS), 2011 IEEE/RSJ International Conference (pp. 1140–1145).

Thomasson, P. G., & Woolsey, C. A. (2013). Vehicle motion in currents. IEEE Journal of Oceanic Engineering, pp, 99–1.

Thomsen, J. E., Guillory, V. G., & Benes, T. A. (2007). The navy unmanned surface vehicle (USV) master plan.

Toussaint, G. J., Basar, T., & Bullo, F. (2000). Tracking for nonlinear underactuated surface vessels with generalized forces. In IEEE Conference on Control Applications, Anchorage, AK.

Woolsey, C. A. (2011). Vehicle dynamics in currents. Technical Report VaCAS-2011-01, Virginia Center for Autonomous Systems, Blacksburg, VA.

Xu, B., Kurdila, A., & Stilwell, D. (2009). A hybrid receding horizon control method for path planning in uncertain environments. In Intelligent Robots and Systems, 2009, IROS 2009, IEEE/RSJ International Conference (pp. 4887–4892).

Yoon, H. K., & Rhee, K. P. (2003). Identification of hydrodynamic coefficients in ship maneuvering equations of motion by estimation-before-modeling technique. Ocean Engineering, 30, 2379–2404.

Yoon, H. K., Son, N. S., & Lee, C. M. (2004). Estimation of roll related hydrodynamic coefficients through the free running model tests. In OCEANS '04. MTTS/IEEE TECHNO-OCEAN '04 (Vol. 2, pp. 1086–1092).

Yu, Z., Bao, X., & Nonami, K. (2008a). Course keeping control of an autonomous boat using low cost sensors. Journal of System Design and Dynamics, 2(1), 389–400.

Yu, Z., Bao, X., & Nonami, K. (2008b). Course keeping control of an autonomous boat using low cost sensors. Journal of System Design and Dynamics, 2(1), 389–400.

15564967, 2013, 30, Downloaded from https://onlinelibrary.wiley.com. By Universita Di Pavia- on [25/11/2021]. Re-use and distribution is strictly not permitted, except for Open Access articles